ADVANCING EARTH AND SPACE SCIENCES

Water Resources Research

RESEARCH ARTICLE
10.1029/2025WR042150

Key Points:

- Amplification effect of cascading dam failure is attributed to downstream dam failure under unsteady flow from upstream dam failure
- Three amplification mechanisms are identified based on the downstream reservoir volume and the timing of downstream dam failure
- The characteristics of landslide dam failure under steady and unsteady flow conditions are compared and analyzed

Supporting Information:

Supporting Information may be found in the online version of this article.

Correspondence to:

D. Shen,
shendanyi@zju.edu.cn

Citation:

Yang, J., Shen, D., Guan, S., Ma, C., Shi, Z., & Soares-Frazão, S. (2026). Amplification of outburst floods during cascading landslide dam failures: Insights from numerical and experimental modeling. *Water Resources Research*, *62*, e2025WR042150. https://doi.org/10.1029/2025WR042150

Received 2 SEP 2025
Accepted 21 JUN 2026

Author Contributions:

Conceptualization: J. Yang
Data curation: J. Yang, D. Shen, S. Guan, C. Ma
Formal analysis: J. Yang, D. Shen
Investigation: S. Guan, C. Ma
Methodology: J. Yang, D. Shen
Software: J. Yang, S. Soares-Frazão
Supervision: Z. Shi, S. Soares-Frazão
Validation: D. Shen
Writing – original draft: J. Yang
Writing – review & editing: D. Shen, Z. Shi, S. Soares-Frazão

Amplification of Outburst Floods During Cascading Landslide Dam Failures: Insights From Numerical and Experimental Modeling

J. Yang[1,2,3], D. Shen[4], S. Guan[5], C. Ma[3], Z. Shi[3], and S. Soares-Frazão[2]

[1]Institute for Water and Environment, Karlsruhe Institute of Technology, Karlsruhe, Germany, [2]Institute of Mechanics, Materials and Civil Engineering, Université Catholique de Louvain, Louvain-la-Neuve, Belgium, [3]Department of Geotechnical Engineering, College of Civil Engineering, Tongji University, Shanghai, China, [4]College of Civil Engineering and Architecture, Institute of Geotechnical Engineering, Zhejiang University, Hangzhou, China, [5]Zhejiang-Greece International Joint Laboratory for Digitial Geotechniques and Intelligent Exploration, Shaoxing University, Shaoxing, China

Abstract Landslide dam failures can trigger catastrophic outburst floods in downstream regions. During cascading dams' failure, a notable amplification in flood magnitude is often observed. However, the mechanisms and influencing factors behind this amplification effect remain unclear. This study investigates the phenomenon through laboratory experiments and numerical simulations involving single and cascading failures of two adjacent landslide dams. The effects of upstream inflow, dam spacing, relative dam height, and material composition are systematically analyzed through three parameters: the discharge amplification index (Q_{am}), the reservoir impounding time (T_{im}) and breach development time (T_b) of the downstream dam. Results indicate that higher upstream inflow rate shortens both T_{im} and T_b, increasing the peak discharge of downstream dam but decreasing Q_{am}. The distance and relative height between the dams influence downstream reservoir volume and breach timing, leading to complex variations in Q_{am}, T_{im}, and T_b. As the median diameter of the downstream dam material increases, T_{im} remains nearly constant, while Q_{am} decreases and T_b increases. Three distinct amplification modes are then identified, each governed by different mechanisms and associated with variations in downstream reservoir volume and failure timing. Moreover, the unsteady flow generated by the upstream dam's failure controls downstream dam failure by increasing erosion rate and decreasing T_b, thereby enlarging the peak discharge and enhancing the amplification effect. These findings clarify the mechanism of amplification effect during cascading dam failure and contribute to hazard management in mountainous regions worldwide.

1. Introduction

The formation of landslide dams is a common natural hazard in mountainous regions worldwide and it occurrence is rapidly growing in response to climate change in recent decades (Carrivick & Tweed, 2016; Shugar et al., 2020; Yanites et al., 2025). It is normally formed with the blockage of river channel by landslide, rockfall or debris flow that is triggered by earthquake or heavy rainfall (Casagli et al., 2003; Costa & Schuster, 1988; Korup, 2004). The sudden failure of landslide dams can lead to catastrophic disasters to local areas and significantly alter the river morphology (Ermini & Casagli, 2003; Veh et al., 2022; Walder & O'Connor, 1997). For example, the failure of the Tangjiashan landslide dam, which was triggered by the 2008 Wenchuan earthquake in southwestern China, deposited several meters of sediments and redirected the Tongkou River near the old Beichuan County (Liu et al., 2010). The outburst flood induced by the failure of the second Baige landslide dam in 2018 endangered nearly 20,000 residents and resulted in substantial economic loss in China (J. Yang et al., 2022). Similarly, the Sikkim flood in 2023, triggered by the failure of the South Lhonak Lake, led to 55 deaths and 74 persons of missing in India (Sattar et al., 2025).

Among these events, a particularly dangerous phenomenon is the formation of cascade landslide dams. This occurs when a second landslide dam forms upstream, downstream or even the same location of the first one. Notable examples include the two landslide dams along the Mianyuan River triggered by the Wenchuan earthquake in Sichuan Province, China, in 2008 (S. Chen et al., 2018); the cascade landslide dams triggered by debris flow events on 8 August 2010, in Gansu Province, China (Takayama et al., 2021; Zhou et al., 2015); the multi-lake outburst flood in the Santa Cruz Valley in Perú (Mergili et al., 2018); and a series of landslide dams formed by the

10.1029/2025WR042150

Kaikoura earthquake on 14 November 2016, in northeastern New Zealand's South Island (Abad et al., 2022). In particular, the Usoi landslide dam, formed in 1911 in the Pamir mountains of Tajikistan, has remained stable for over a century, but a potential for cascading failure in the future still exists (Nardini et al., 2024). In such cases, the failure of the upstream dam releases a strong unsteady flow that accelerates the failure of the downstream dam, resulting in distinct failure patterns and the amplification effect that significantly increases the intensity of downstream flooding (Cui et al., 2013; Geertsema et al., 2022; Zhou et al., 2013).

As a landslide dam can be considered similar to an earthen embankment formed without proper layering and compaction, research on the failure of a single landslide dam can be conducted by investigating laboratory dam-breaching experiments (Coleman et al., 2002; Gregoretti et al., 2010; Guan et al., 2023; Morris et al., 2008; Rifai et al., 2017; Shen et al., 2024; Walder et al., 2015; Zhou et al., 2022). With this point of view, numerical studies also provide valuable insights into the failure processes (Cao et al., 2011; Dazzi et al., 2019; Ferrari et al., 2023; J. Yang et al., 2024; Zhong et al., 2018). These studies provide not only abundant data resources for analyzing the dam failure pattern, the discharge variation and the breach development, but also efficient methods to simulate and predict the influence on local areas of such events. Similar experimental and numerical methods are also used to analyze the cascading failure of landslide dams. The results are compared with those considering single landslide dams. For example, flume experiments at different scales considering varying parameters such as the distance between two cascade landslide dams, the dam geometry and the dam material composition were conducted to assess their impact on the amplification effect caused by the cascading failure of landslide dams (Hu et al., 2022; Zheng et al., 2022; Zhou et al., 2013). These studies indicated that, compared to the failure of a single landslide dam, a significant increase in peak discharge is observed during the failure of the downstream dam in cascading events, along with distinct dam failure patterns. However, the mechanisms associated with the amplification effect and the failure patterns during cascading landslide dam failures remain unclear, and there is no systematical analysis using varying parameters. Further data are needed to enable a more comprehensive analysis of cascading landslide dam failures.

In terms of numerical simulation, two different types of numerical models, simplified and detailed physically-based numerical models, are used to simulate the cascading failure of landslide dams (Dai et al., 2025; Schmitz et al., 2023; van de Bout et al., 2022). For example, Shi et al. (2015) further developed the simplified model DABA, originally proposed by Chang and Zhang (2010), to simulate the cascading failures, including those of the Tangjiashan and the downstream Kuzhu dams. Cao et al. (2011) and Q. Yang et al. (2020) conducted numerical simulations in an experimental scale based on the detailed numerical models to analyze the amplification effect caused by the cascading failure of landslide dams. Research on selecting appropriate parameters in numerical simulations also contribute to achieving better agreement between numerical results and real-world scenarios (AI Mehedi et al., 2024; Haces-Garcia et al., 2025). These studies verified the applicability and accuracy of these models in simulating the cascading failure of landslide dams. Moreover, the numerical models can provide abundant results compared to the flume experiments, aiding us to analyze the mechanism of amplification effect and its relationship with the dam failure patterns. However, these models ignore the characteristics of dam material composition or consider these factors using assumed dam failure patterns and empirical equations, leading to inaccurate simulations of the actual dam failure process, and to very poor predictive capabilities. Taking into account the failure characteristics of landslide dams, we developed a detailed numerical model considering multi-layered, non-uniform sediments, and also a bank failure module to simulate landslide dam failure (J. Yang et al., 2024). The applicability and accuracy of the proposed model was verified with both experimental results and those from real scenarios (J. Yang et al., 2024, 2025). This new model finally allowed us to better simulate and understand the dam failure pattern and the amplification effect of the outburst flooding.

In this paper, we aim to solve the following two questions: (a) Which factors control the failure process and the associated amplification effect during cascading landslide dam failure? (b) How do these factors influence the amplification effect (the mechanism of the amplification effect)? To answer these two questions, the proposed two-dimensional shallow water based numerical model (J. Yang et al., 2024) is employed to simulate the cascading failure of landslide dams. The dam failure patterns and the amplification effects associated with the downstream flooding considering varying parameters are systematically analyzed. The paper is organized as follows: Section 2 introduces the numerical model, experimental setup, numerical scenarios and configurations. Section 3 presents the calibration of the model and the main observations. Section 4 discusses the key factors influencing the amplification effect, and dam failure characteristics under steady and unsteady flow conditions. Finally, the conclusions arising from the current work are described in Section 5.

10.1029/2025WR042150

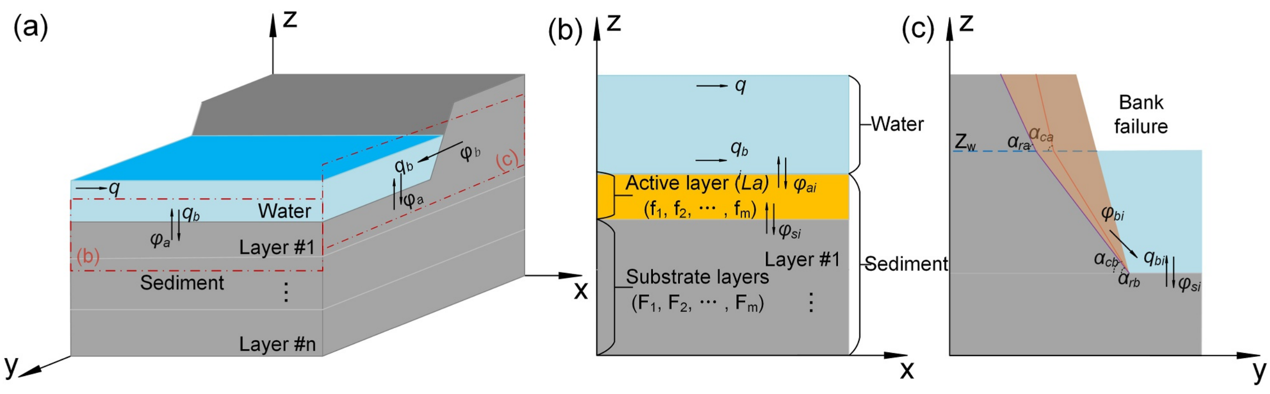

Figure 1. Hydro-morphodynamical model considering non-uniform and multi-layered sediment: (a) overview of the model; (b) the active layer module and (c) the bank failure module. Note: q is the discharge, q_b and q_{bi} are the bedload transport rate for the total sediment and for each fraction of the sediment. φ_a and φ_b are the interactions of bedload with sediment bed and bank material, respectively. φ_{ai} and φ_{bi} are the interaction of bedload with each fraction of the sediment bed and bank material. φ_{ai} is the interaction between the active layer and substrate layer in each fraction of the sediment. α_{ca} and α_{cb} are the critical angles above and below the water level. α_{ra} and α_{rb} are the residual angles above and below the water level Z_w (J. Yang et al., 2025).

2. Materials and Methods

2.1. Numerical Model

The two-dimensional hydro-morphodynamical model, developed by J. Yang et al. (2024), is employed here for numerical simulation. This model builds upon the hydrodynamic framework WATLAB (Soares-Frazão et al., 2012), integrating a sediment algorithm that accounts for non-uniform and multi-layered sediment characteristics (Figure 1). The model solves the shallow water equations to update the flow information during dam failure. To track sediment dynamics, the model uses the modified Exner equation in conjunction with the MPM formula, enabling updates to sediment depth and computation of bed fluxes within an active layer on the surface of the sediment bed. The sediment in the active layer is further divided into multiple fractions and changes in material composition are calculated through interactions among bedload fluxes, the active layer and underlying substrate layers, using the Hirano's active layer equation (Figure 1b). Additionally, a bank failure module proposed by Swartenbroekx et al. (2010) is incorporated to simulate the breach development during dam failure (Figure 1c). The model is solved based on a weakly-coupled finite volume scheme (Meurice & Soares-Frazão, 2020) considering unstructured triangular mesh. Full details of the numerical model regarding the governing equations, the numerical schemes, boundary and initial conditions are provided in Supporting Information S1, and the model application for simulating landslide dam failure is discussed in J. Yang et al. (2024, 2025).

2.2. Flume Tests of Cascading Failure of Landslide Dams

Three flume tests, including two single landslide dam failures with varying material compositions and a cascading dam failure, were conducted at Tongji University, China. These flume tests were further used to calibrate the numerical model and to validate the results in associated with cascading dam failure. The flume has a rectangular design, measuring 50 m in length, 0.8 m in width, and 1.25 m in height (Figures 2a and 2b). A water tank is connected to both the upstream and downstream ends to provide the desired inflow rate and recirculate water within the flume. The flume base is constructed from steel with a zero gradient, while the side walls are made of organic tempered glass to facilitate observation.

The single dam failure tests involved one dam located 26.50 m downstream from the flume inlet, that is, at the location of the second dam from the cascading experiments. This dam has a height of 0.9 m, a top width of 0.5 m, and a bottom width of 3.62 m (Figures 2c and 2e). Two different material compositions are considered: fine-dominated and well-mixed materials (Figure 3a), were considered. These two materials consist of sand and gravel with particle sizes ranging from 0.005 to 60 mm, with varying percentage contents based on the composition type. A constant upstream inflow rate of 1.13 L/s was maintained throughout all single dam failure experiments (T1 and T2) considering fine-dominated (FD) and well-mixed materials (WM). For the cascading

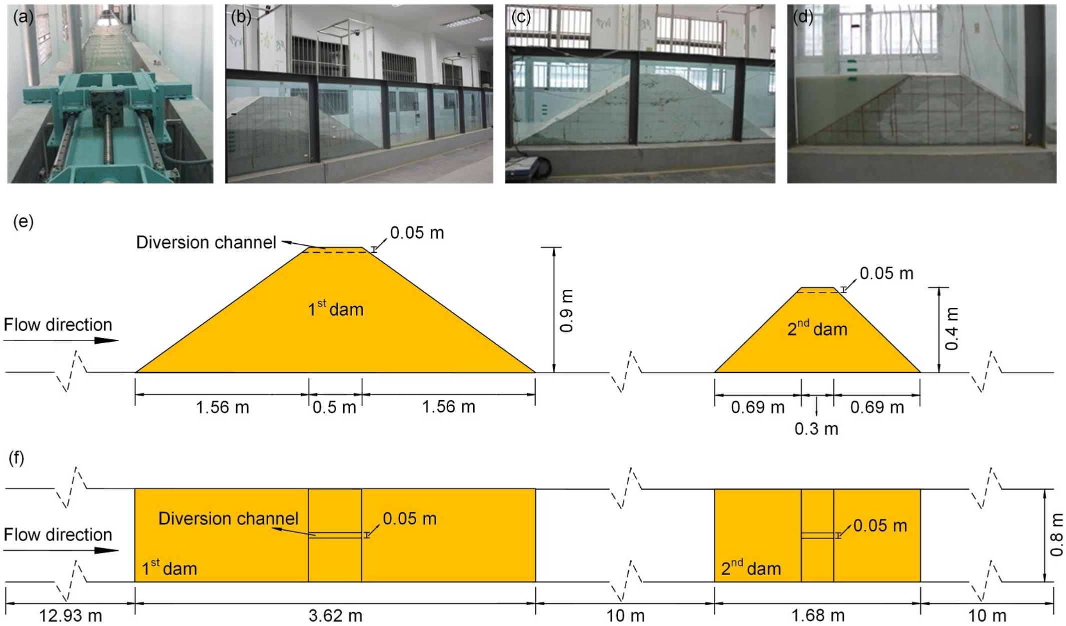

Figure 2. Experimental setup: (a), (b) the flume at Tongji University; (c), (d) the modeled dams; (e) cascading experimental design from side view and (f) from top view.

dam failure test (T3), two dams made of the same material but differing in geometry were constructed along the flume. The upstream dam in this test is identical in geometry to the single dam failure tests but located at 12.93 m downstream from the inlet. The downstream dam, situated 10 m downstream from the first, is smaller, with a height of 0.4 m, a top width of 0.3 m, and a bottom width of 1.69 m (Figures 2d–2f). Additionally, rectangular diversion channels with a top width of 0.05 m and a depth of 0.05 m were constructed on the crest of all the model dams. The cascading dam failure test used fine-dominated material for both dams and a constant inflow rate of 1.13 L/s in the upstream. It should be noted that the geometry, upstream reservoir and dam material composition of landslide dams in natural environment vary significantly in response to the local geological condition, the river condition, etc. (see Text S2 in Supporting Information S1). Therefore, the modeled dam in the experiments does not exactly correspond to a given prototype case. However, we considered the shape of the Tangjiashan landslide dam (Fan et al., 2012) and a geometrical scaling of 1:100 to determine the height, width, and length of the dam, as well as the upstream reservoir. The basic parameters of the three tests are summarized in Table 1.

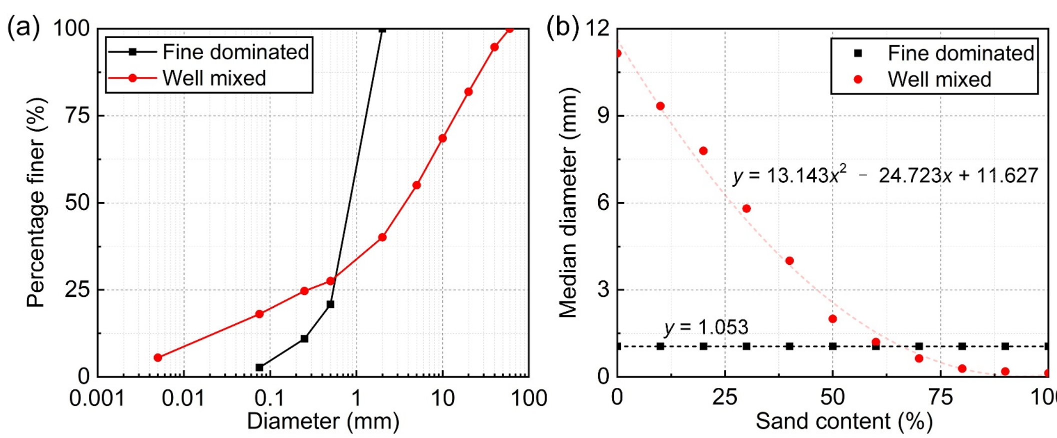

Figure 3. Experimental dam materials: (a) Grain size distribution of the three dam materials; (b) Relationship between sand content and median diameter.

Table 1
Basic Parameters of the Three Experimental Tests

		Material								
Test	Failure type	Type	d_{50}	S_c	ρ_d	φ	C_u	C_c	e	Q_{in}
T1	Single	Fine-dominated	1.05	100.00	1.78	27	5.5	1.2	0.488	1.13
T2		Well-mixed	3.99	40.10	1.78	38	61.3	0.7	0.488	1.13
T3	Cascade	Fine-dominated	1.05	100.00	1.78	27	5.5	1.2	0.488	1.13

Note. d_{50} (mm) is the median diameter of the material. S_c (%) is the sand content of the material. ρ_d (g/cm^3) is the dry bulk density. φ (°) is the angle of repose. $C_u = d_{60}/d_{10}$ and $C_c = d_{30}$^2/(d_{60}*d_{10}) are the uniformity coefficient and curvature coefficient. e is the void ratio and Q_{in} is the upstream in flow rate (L/s).

2.3. Numerical Scenarios and Setup

The composition of dam materials, along with parameters such as the Manning coefficient and median diameter, significantly influence the dam failure process and the accuracy of the numerical simulations (Martínez-Aranda et al., 2022; Schmitz et al., 2023; Wu, 2013). To ensure the accuracy of the numerical results, three numerical tests corresponding to flume experiments of both single and cascading dam failures were conducted to calibrate and validate the numerical model. Simulations employed an unstructured triangular mesh with mesh size ranging from 0.05 to 0.1 m. The non-uniform dam materials were categorized into two groups during the simulation: sand with diameters smaller than 2 mm, and gravel for larger particles. Polynomial regression fitting curves between sand content and median diameter of each material (Figure 3b) were used to model variations in surface grain size distribution during dam failure. Therefore, the relationship between sand content and the median diameter of the dam materials can be expressed as follows:

$$d_{50} = \begin{cases} 13.143{P_S}^2 - 24.723P_S + 11.627 & \text{for WM} \\ 1.053 & \text{for FD} \end{cases} \tag{1}$$

where P_S is the sand content of dam material and d_{50} is the median diameter. Regarding the Manning coefficient, as different sediment fractions are considered, it is necessary to calculate a global value based on the representative diameters of each fraction, which can be expressed as follows (J. Yang et al., 2025):

$$n = \left(\sum_{i=1}^{N} P_i \left(d_{50,i}^{1/6} / A_n \right)^{3/2} \right)^{2/3} \tag{2}$$

where P_i (%) and $d_{50,i}$ (mm) are the percentage content and median diameter of each sediment fraction. $A_n = 16$ is an empirical coefficient, N is the number of sediment fraction. Details about the equation can be accessed via Text S3 in Supporting Information S1. Specific parameters for the numerical tests are listed in Table 2.

Table 2
Numerical Scenarios and Parameters for Calibrating the Numerical Model

							P_i		$d_{50,i}$		Bank failure			
Test	L	d_{50}	s	n	f	F	S	G	S	G	α_{ca}	α_{cb}	α_{ra}	α_{rb}
T1	1	1.05	2.65	0.022	0.328	2	100	0	1.05	–	60	31	60	31
T2	1	3.99	2.65	0.024	0.328	2	40.1	59.9	0.13	11.15	75	38	75	38
T3	1	1.05	2.65	0.022	0.328	2	100	0	1.05	–	60	31	60	31

Note. L is the number of sediment layer. d_{50} (mm) is the median diameter. s is the relative specific gravity. n (sm$^{-1/3}$) is the Manning coefficient. f is the porosity. F is the number of sediment fraction in each layer. P_i (%) and $d_{50,i}$ (mm) are the percentage content and median diameter of each sediment fraction. S and G are sand and gravel, respectively. α_{ca} and α_{cb} are critical angles above and below water level, respectively. α_{ra} and α_{rb} are residual angles above and below water level, respectively.

After calibrating the numerical model with two single dam failure experiments (T1 and T2) and validating with the cascading dam failure experiment (T3), 34 scenarios were run to investigate the cascading failures of the two modeled dams. Details of the numerical scenarios are summarized in Table 3. In these scenarios, five upstream inflow rates, represented by Q_{in}/Q ($Q = 1.13$ L/s), ranging from 0.5 to 2.5 were considered. The relatively dam height, which was defined as H_d/H (Hd are dam height of downstream dam and $H = 0.4$ m as considered in the experiment), and the distance between two dams (D), varied from 2.5 to 12.5 m. In particular, the upstream dam is located at the same position in all the scenarios, and its height remains constant to ensure that the same upstream reservoir volume (V_u) is observed in different scenarios. For the material compositions in the numerical scenarios, fine-dominated material is considered in the upstream dam in all scenarios, while in S30–S34, the downstream dams are composed of well-mixed materials, so as to analyze the influence of material composition on cascading dam failure.

2.4. Data Analysis

The numerical results are analyzed from two aspects: (a) calibration and validation of the numerical model, and (b) the amplification effect induced by cascading dam failure. For model calibration, single-dam failure experiments are used, focusing on discharge variation and breach development along and across the river channel. After calibration, the model is validated against cascading dam failure by comparing the downstream dam failure process and the discharge variations of both dams. In particular, the accuracy of the dam breach hydrograph is quantitatively evaluated using the Kling-Gupta Efficiency (KGE), while the breach development during dam failure is evaluated using the Root Mean Square Error (RMSE). These two parameters are calculated considering the discharge during dam failure, the breach depth at several time steps and the final breach width, and can be expressed as follows:

$$\mathrm{KGE} = 1 - \sqrt{\left(\frac{\sum(Q_{\mathrm{et}} - \overline{Q_{\mathrm{et}}})(Q_{\mathrm{nt}} - \overline{Q_{\mathrm{nt}}})}{\sqrt{\sum(Q_{\mathrm{et}} - \overline{Q_{\mathrm{et}}})^2}\sqrt{\sum(Q_{\mathrm{nt}} - \overline{Q_{\mathrm{nt}}})^2}} - 1\right)^2 + \left(\frac{\sqrt{\frac{1}{M}\sum(Q_{\mathrm{nt}} - \overline{Q_{\mathrm{nt}}})^2}}{\sqrt{\frac{1}{M}\sum(Q_{\mathrm{et}} - \overline{Q_{\mathrm{et}}})^2}} - 1\right)^2 + \left(\frac{\overline{Q_{\mathrm{nt}}}}{\overline{Q_{\mathrm{et}}}} - 1\right)^2} \quad (3)$$

$$\mathrm{RMSE}(B_D) = \sqrt{\frac{1}{M}\sum(B_{D\mathrm{nt}} - B_{D\mathrm{et}})^2}, \qquad \mathrm{RMSE}(B_W) = \sqrt{\frac{1}{M}\sum(B_{W\mathrm{nt}} - B_{W\mathrm{et}})^2} \quad (4)$$

where Q_{et} and Q_{nt} are the discharge at time t in response to experimental and numerical results, respectively. B_D and B_W refer to the breach depth and breach width, respectively. M is the number of the data point.

Regarding the amplification effect, three parameters are considered: the discharge amplification index (Q_{am}), the impounding time of the second dam (T_{im}) and the time for breach development (T_b). Specifically, Q_{am} represents the ratio of the peak discharge from the second dam to that of the first dam, T_{im} is defined as the time interval between the overflow of the first dam and the onset of overflow at the second dam, and T_b is defined as the duration from the start of overflow at the second dam to the occurrence of its peak discharge. These three parameters can be calculated as follows:

$$Q_{\mathrm{am}} = \frac{Q_{p\_\mathrm{down}}}{Q_{p\_\mathrm{up}}} \quad (5)$$

$$T_{\mathrm{im}} = T_{o\_\mathrm{down}} - T_{o\_\mathrm{up}} \quad (6)$$

$$T_b = T_{p\_\mathrm{down}} - T_{\mathrm{im}} \quad (7)$$

where Q_{p_down} and Q_{p_up} are the peak discharge during the failure of the downstream and upstream dams, respectively. T_{o_down} and T_{o_up} are the times when the downstream and upstream dams start to overflow, respectively, and T_{p_down} is the time interval between the overflow of the first dam and the time when the peak discharge is observed during the failure of the downstream dam.

10.1029/2025WR042150

Table 3
Numerical Scenarios With Varying Inflow Rates, Material Compositions, Distances and Relatively Heights Between Two Dams

	Parameters			Materials	
Scenarios	Q_{in}/Q	H_d/H	D (m)	1st dam	2nd dam
S1	0.5	1.0	10.0	FD	FD
S2	1.0				
S3	1.5				
S4	2.0				
S5	2.5				
S6	1.0	0.5	2.5	FD	FD
S7			5.0		
S8			7.5		
S9			10.0		
S10			12.5		
S11	1.0	1.0	2.5	FD	FD
S12			5.0		
S13			7.5		
S14			12.5		
S15	1.0	1.5	2.5	FD	FD
S16			5.0		
S17			7.5		
S18			10.0		
S19			12.5		
S20	1.0	2.0	2.5	FD	FD
S21			5.0		
S22			7.5		
S23			10.0		
S24			12.5		
S25	1.0	2.5	2.5	FD	FD
S26			5.0		
S27			7.5		
S28			10.0		
S29			12.5		
S30	1.0	1.5	2.5	FD	WM
S31			5.0		
S32			7.5		
S33			10.0		
S34			12.5		

Note. Q_{in}/Q is the non-dimensional inflow rate, with $Q = 1.13$ L/s, H_d/H is the non-dimensional downstream dam height, with $H = 0.4$ m, D is the distance between two dams; FD and WM refer to the fine-dominated and well-mixed materials.

3. Results

3.1. Calibration of the Numerical Model Considering Single Dam Failures

Figure 4 presents both the numerical and experimental results for discharge variation during the failure of a single dam with different material compositions. The Kling-Gupta Efficiency (KGE) for the scenario considering fine-dominated material (T1) is 0.929, and a value of 0.627 is obtained for the well-mixed material scenario (T2). Both KGEs are larger than 0.5, indicating a good agreement between numerical results and experimental data. For the fine-dominated dam, overflow of the diversion channel began 535 s after the simulation started, with the peak discharge occurring 510 s later. The peak discharge was estimated at 0.132 m^3/s, showing a 2.2% deviation from the experimental value of 0.135 m^3/s. In the case of the well-mixed material dam, overflow occurred at 550 s, which is comparable to the fine-dominated case due to identical reservoir volume and dam geometry. The simulated peak discharge was 0.073 m^3/s, closely matching the experimental value of 0.074 m^3/s, with a difference of only 1.35%. Furthermore, the well-mixed dam exhibited a significantly longer time interval between the onset of overflow and peak discharge (1,080 s vs. 510 s), and a notably lower peak discharge (0.073 m^3/s vs. 0.132 m^3/s), indicating a more gradual failure process compared to the fine-dominated dam.

The differences in dam failure duration and peak discharge between the two material compositions are primarily governed by the breach development process. This process can be characterized by the evolution of breach geometry, specifically, the widening of the breach and the reduction of dam height within the breach zone. Figure 5 illustrates the dam failure progression for both fine-dominated and well-mixed material compositions. For the fine-dominated dam (Figures 5a–5f), the breach depth increased gradually from the onset of overflow until approximately 840 s into the simulation (Figure 5c). After this point, both breach depth and width expanded significantly (Figures 5d and 5e), resulting in a rapid increase in discharge. Following the peak discharge, the dam height notably decreased along the flow direction (Figures 5e and 5f), indicating substantial erosion within the breach. In contrast, the well-mixed dam (Figures 5g–5l) exhibited minimal change in breach geometry up to 1,030 s after the start of the simulation. Thereafter, both breach depth and width began to increase simultaneously. Similar to the fine-dominated dam, the maximum breach width was reached prior to the peak discharge (Figure 5j). However, the breach development in the well-mixed dam progressed more slowly, resulting in the formation of a localized erosion hole downstream of the dam (Figure 5k). This erosion hole was subsequently refilled with sediment after the peak discharge, and a higher residual dam body remained compared to the fine-dominated case (Figure 5l).

Regarding the breach development, it progresses more slowly and progressively in the numerical simulations than in the experiments (Figures 6a and 6b). The RMSEs for the two scenarios considering fine dominated material (T1) and well-mixed material (T2) are 0.151 and 0.085 m, respectively. This discrepancy is mainly attributed to the simplified bank failure module implemented in the model (Figure 1c), which neglects the influence of unsaturated soil behavior and therefore fails to capture sudden slope collapses that occur during dam failure. Despite this limitation, the model successfully reproduces the onset of breach widening and the final breach geometry for both fine-dominated and well-mixed material cases. With regard to the longitudinal dam profile, the model accurately captures the variation in dam height at the upstream dam crest (RMSE = 0.037 m for T1 and 0.076 m

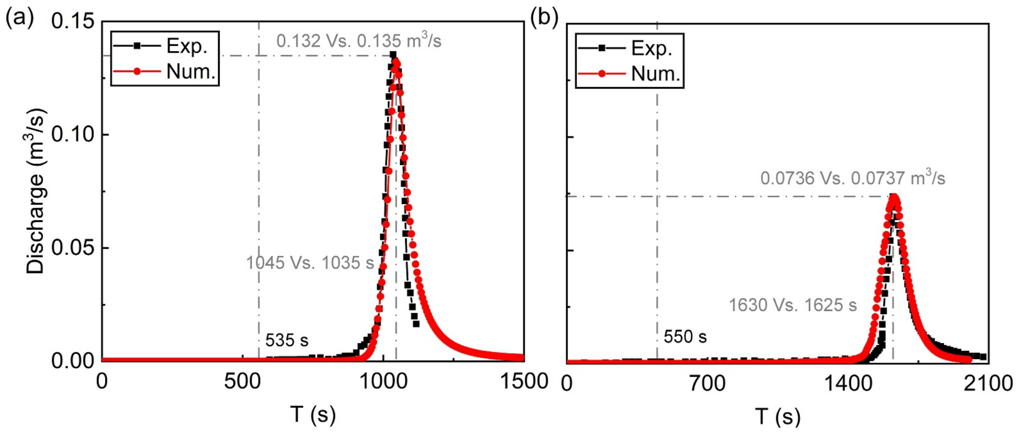

Figure 4. Comparison of discharge variation during dam failure with varying material compositions: (a) fine dominated material composition (T1) and (b) well-mixed material composition (T2).

for T2), which is an essential factor controlling discharge variation during dam failure. Nevertheless, certain limitations remain. For example, the model failed to reproduce the steeper erosion surface (Figure 6c) and the stepped erosion surface (Figure 6d) observed in the experiment. Such features are typical of more cohesive materials, and are not accounted for in the numerical model. Despite these differences, the good agreement in dam crest evolution and the final dam profile indicates that the numerical model performs reasonably well in simulating single dam failures with varying material compositions.

3.2. Numerical Validation of Cascading Dam Failure

Numerical results of cascading dam failure are shown in Figure 7. The simulated discharge curves for both the upstream and downstream dams show good agreement with the experimental data (Figure 7a), with KGE values of 0.844 and 0.943, respectively. The peak discharges are 0.053 and 0.105 m^3/s, with deviations of 1.92% and 1.94%, respectively, from the experimental values of 0.052 and 0.103 m^3/s. Additionally, the time interval between the two peak discharges is estimated to be 40 s, closely matching the experimental observation of 47 s. Regarding the longitudinal failure process of the downstream dam, the numerical model accurately captures the dam height variation (RMSE = 0.014 m), as observed in single dam failure cases. However, it underestimates the slope of the erosion surface during the failure process (Figure 7b). This discrepancy is more pronounced than in the single dam scenario due to the greater unsteady flow generated by the upstream dam failure. Despite these limitations, the final dam topography from the numerical simulation aligns well with the experimental results. Therefore, the numerical model, along with the parameters adopted for different material compositions, is considered capable of effectively analyzing the characteristics of cascading dam failure.

3.3. Influence of Upstream Inflow

Figure 8 illustrates the variations in discharge and upstream water depth for both the upstream and downstream dams under different inflow rates. Similar trends were observed in both discharge and upstream water depth. The upstream water depth gradually increased until failure occurred, followed by a decrease to a constant level corresponding to the residual dam height. During this process, discharge increased to a peak and then gradually declined until the end of the failure event. For the downstream dam, the upstream water depth began increasing from zero after the first dam failed, reached a maximum, and then decreased as the downstream dam failed. Despite the downstream dam having a smaller height and reservoir volume, it exhibited a steeper discharge curve and a higher peak discharge during failure, resulting in the amplification effect during cascading dam failure. This cascading effect can be attributed to the unsteady flow generated by the upstream dam failure, which significantly intensified the downstream flood, characterizing the downstream dam failure as being driven by transient hydraulic conditions. Regarding the differences in discharge and water depth variations under different inflow rates, a lower inflow rate resulted in a longer impounding time and a smaller peak discharge for the failure of the first dam. In contrast, for the downstream dam, the influence of inflow rate on the cascading effect, particularly the discharge variation, was less evident. This phenomenon indicates that the amplification effect of cascading dam

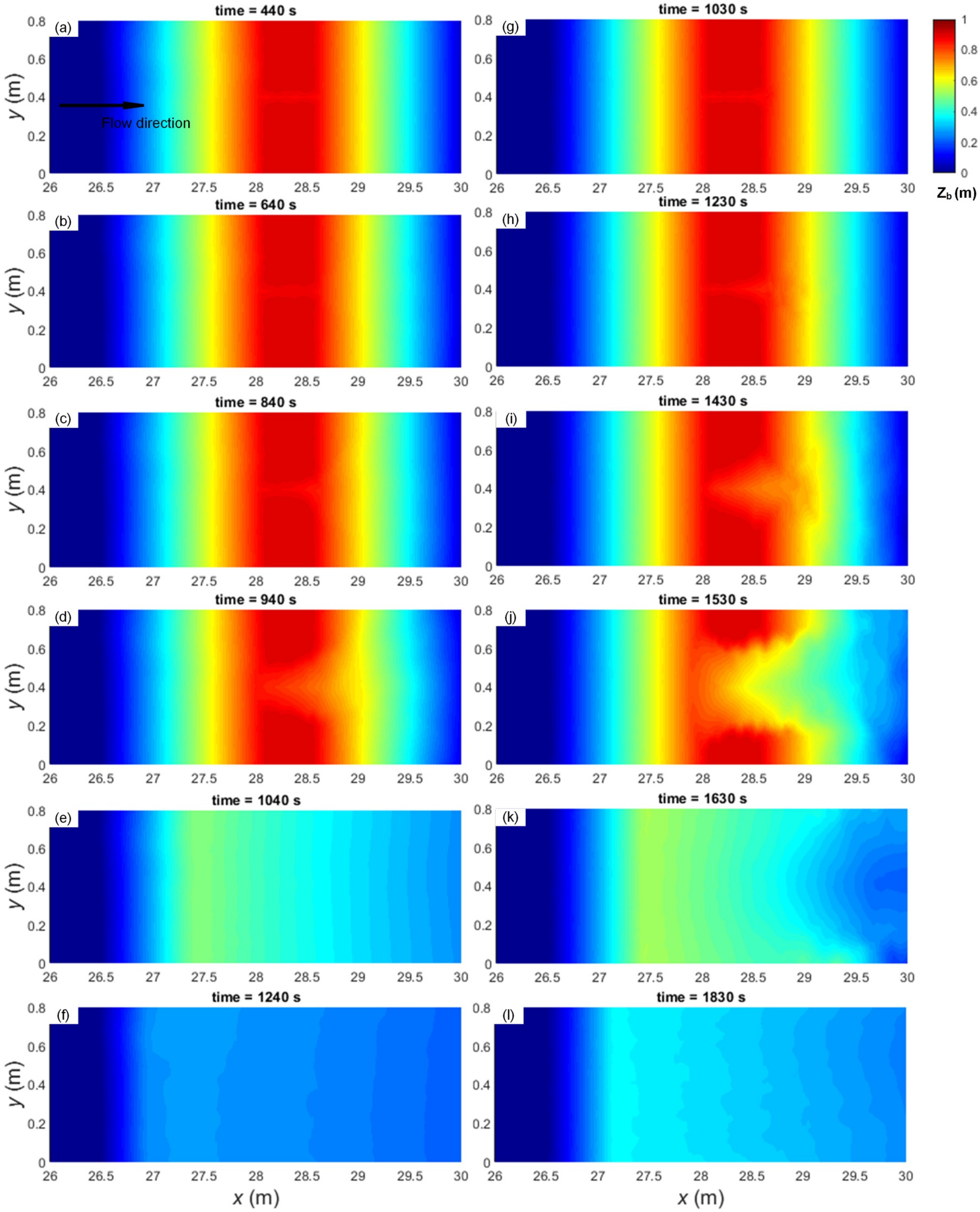

Figure 5. Dam failure process from numerical simulation with varying material compositions: (a)–(f) fine dominated material composition and (g)–(l) well-mixed material composition.

failure is dominated by the water volume that is released during the failure of the first dam under varying upstream inflow rates.

Figure 9 shows the variations in discharge, dam failure duration, and the three defined parameters for both dams during their cascading failure. As the upstream inflow rate increased from 0.000565 to 0.00283 m^3/s, the peak discharge during the failure of both the upstream and downstream dams increased accordingly. Specifically, the

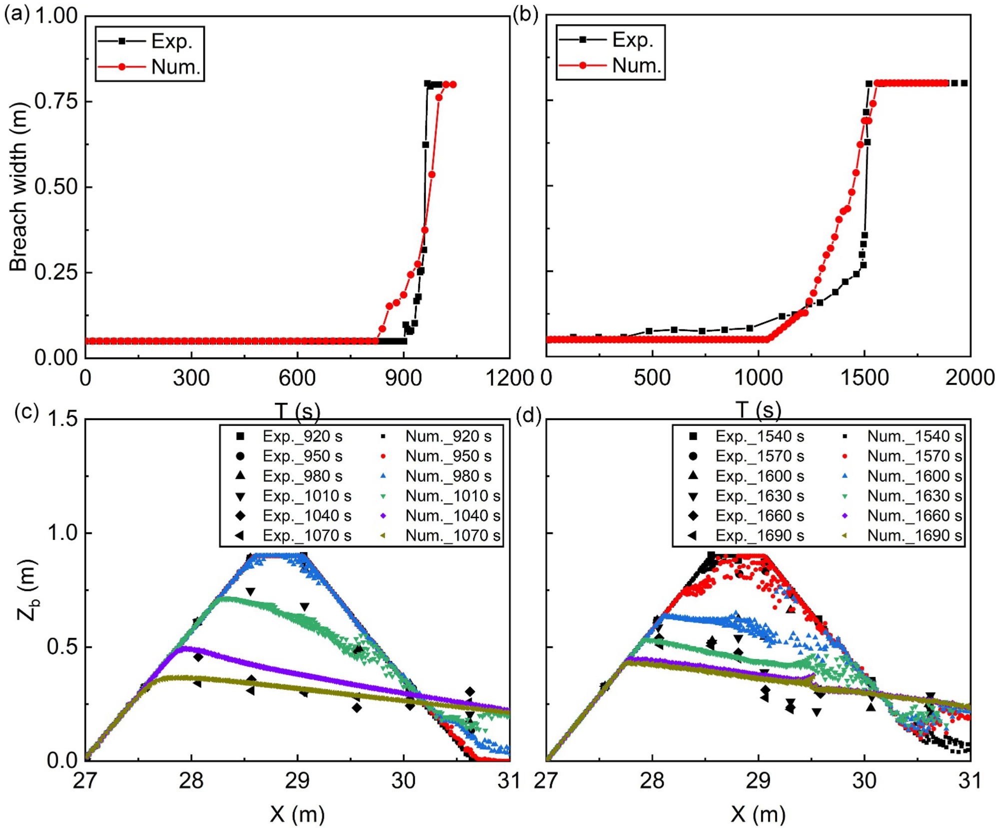

Figure 6. Dam failure process of single dam with varying material compositions: (a), (b) breach evolution of dams considering fine-dominated and well-mixed material compositions, respectively; (c), (d) Longitudinal dam profile evolution considering fine-dominated and well-mixed material compositions, respectively.

peak discharge of the upstream dam changed from 0.050 to 0.068 m^3/s, while that of the downstream dam increased from 0.102 to 0.126 m^3/s. However, the discharge amplification index (Q_{am}) showed a slight decrease with increasing inflow rate. As shown in Figure 9a, Q_{am} was estimated at 2.63 for an inflow rate of 0.000565 m^3/s, and it decreased to 2.12 when the inflow rate reached 0.00283 m^3/s. Regarding the timeline for the failure of the downstream dam, the time required to impound the reservoir of the downstream dam (T_{im}) decreased with increasing inflow, due to the higher discharge generated by the failure of the first dam. Similar decreasing trend was observed for the time to peak discharge (T_{p_down}) and the time for breach development (T_b). In particular, T_{im}

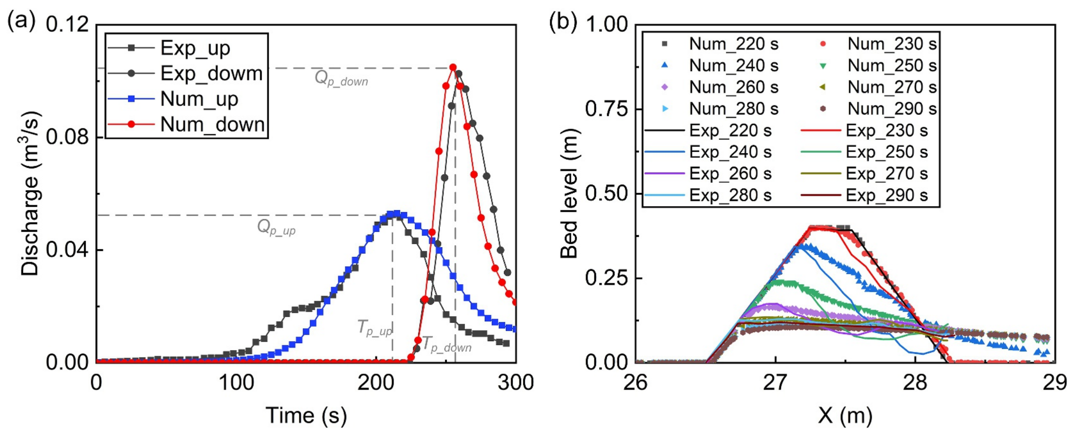

Figure 7. Discharge variation and dam failure process during the cascading failure of two dams: (a) discharge variation of both the upstream and downstream dams, and (b) longitudinal dam failure process of the downstream dam.

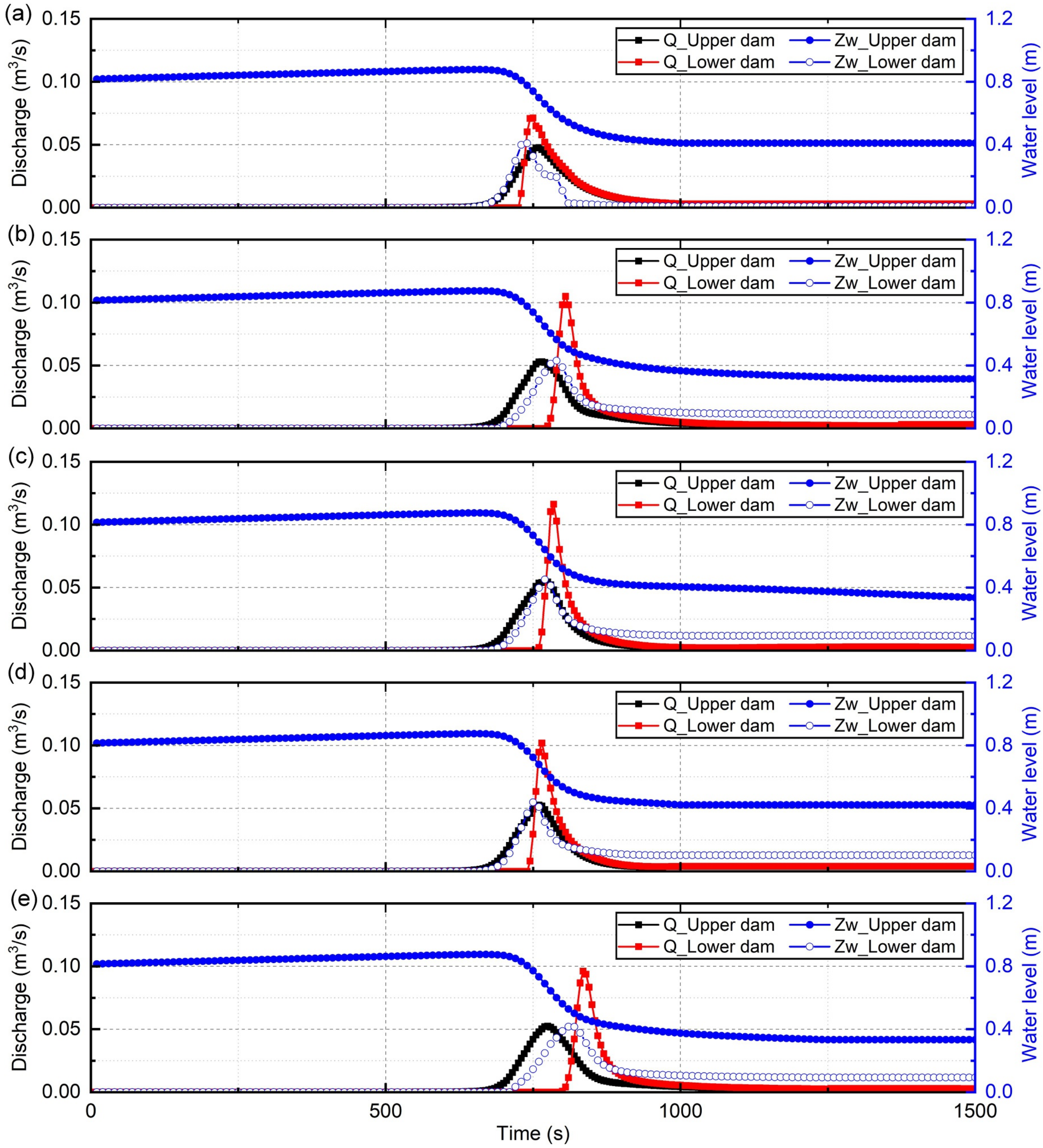

Figure 8. Variation of upstream water level and discharge of both upstream and downstream dams with varying upstream inflows: (a) $Q_{in}/Q = 0.5$; (b) $Q_{in}/Q = 1$; (c) $Q_{in}/Q = 1.5$; (d) $Q_{in}/Q = 2$; (e) $Q_{in}/Q = 2.5$.

decreased from 540 to 225 s and T_b decreased gradually from 40 to 25 s as the upstream inflow rate increased. Overall, under varying upstream inflow rates, the cascading effect of the downstream dam is primarily governed by the unsteady flow induced by the failure of the upstream dam. A higher peak discharge from the upstream dam shortens both the reservoir impounding and breach development times for the downstream dam, resulting in a greater peak discharge from the second dam but a lower discharge amplification index.

3.4. Influence of Distance and Relatively Height of Two Dams

Figure 10 shows the influence of both the distance and the relative height between the two dams on the discharge amplification index (Q_{am}). Under different relative height ratios (H_d/H), the variation of Q_{am} with increasing

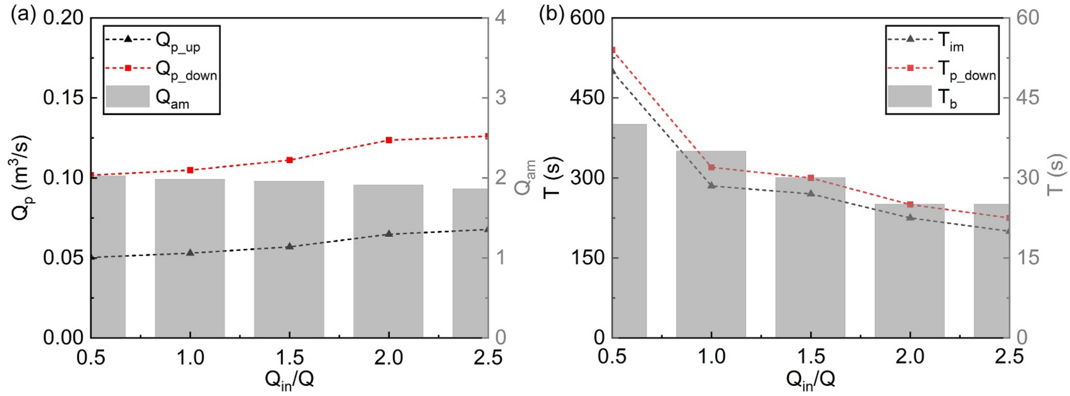

Figure 9. Amplification effect under varying upstream inflows: (a) Variations of peak discharge of both dams and the discharge amplification index; (b) variation of time for impounding downstream dam's reservoir, time to peak discharge and breach development.

distance between the dams showed distinct trends. Specifically, when the relative height was 0.5, 2.0, and 2.3, Q_{am} increased with increasing dam spacing. In contrast, a non-monotonic trend was observed when $H_d/H = 1.0$, where Q_{am} first increased and then decreased. A reversed pattern appeared for $H_d/H = 1.5$, where Q_{am} initially decreased and then increased, as shown in Figure 10a. Regarding the influence of relatively height of two dams on Q_{am} under varying distances between two dams, a similar non-linear pattern was observed. In particular, for $H_d/H = 1.5$ and 2.0, Q_{am} first increased, then decreased, and finally increased again with increasing relative height. To further explain these variations in Q_{am}, four representative scenarios (S2, S6, S17, and S18) were selected for detailed analysis of the discharge and upstream water level variations for both dams (Figure 11). Scenario 2 served as a reference case (Figure 11b), while S6 represented the case with the smallest downstream dam height and the largest dam spacing (Figure 11a). Scenarios 17 and 18 were chosen based on extremes in Q_{am} values: S17 had the lowest Q_{am} observed (Figure 11c), and S18 showed a sudden increase in Q_{am} (Figure 11d).

In the case of the smallest H_d/H and the largest D between the two dams (S6), the downstream dam failed before the peak discharge of the upstream dam was reached (Figure 11a). Consequently, the failure of the downstream dam consistently occurred during the rising limb of the first dam's discharge curve. As the distance between the dams increased, both the discharge at the time of the second dam's failure and the volume of its reservoir increased, resulting in a higher peak discharge for the downstream dam. In some cases, multiple discharge peaks were observed. In contrast, for scenarios S2, S17, and S18, unlike S6, the downstream dam failed during the falling limb of the first dam's discharge curve. Under these conditions, the hydraulic behavior varied significantly among the three scenarios. In S2, the failure of the downstream dam did not influence the upstream dam. With the same downstream dam height, the discharge at the time of the second dam's failure decreased and the downstream

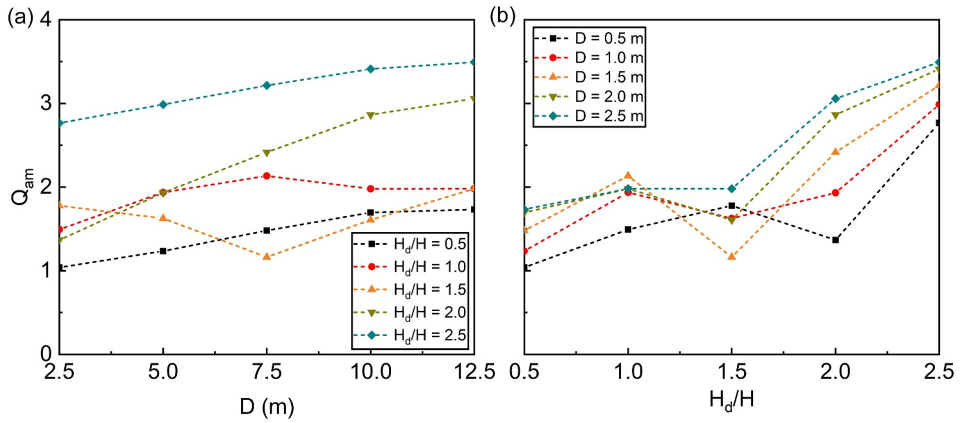

Figure 10. Variation of discharge amplification with varying distances and relatively heights between two dams: (a) influence of distance and (b) influence of relatively height.

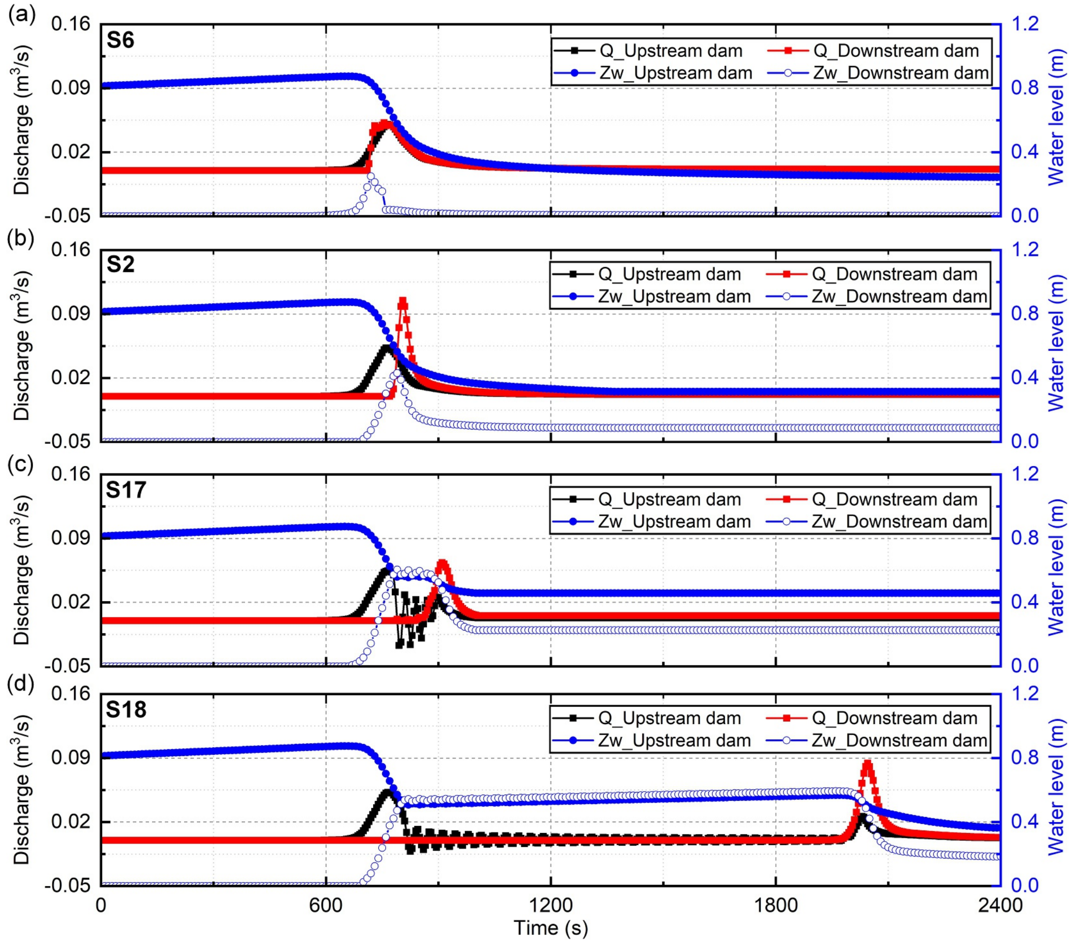

Figure 11. Variation of upstream water level and discharge of both upstream and downstream dams with varying distances and relatively heights between two dams: (a) $D = 2.5$ m, $H_d/H = 0.5$ (S6); (b) $D = 10$ m, $H_d/H = 1$ (S2); (c) $D = 7.5$ m, $H_d/H = 1.5$ (S17); (d) $D = 10$ m, $H_d/H = 1.5$ (S18).

reservoir volume increased as the distance between the dams grew. This led to an initial increase followed by a decrease in Q_{am}, as shown by the red line in Figure 10a. In S17 and S18, however, the downstream dam had a strong influence on the first dam's failure process. Notably, the water level upstream of the downstream dam became equal to that of the upstream dam, causing fluctuations in the discharge curve of the first dam. Under such conditions, the failure of the downstream dam gradually transitioned from a cascading failure to an independent, single dam failure, resulting in the lowest Q_{am} observed. Furthermore, as both the downstream dam height and the distance between the dams increased, the reservoir volume of the downstream dam also increased, ultimately contributing to a gradual rise in Q_{am}.

Figure 12 shows the influence of the relatively height (H_d/H) and the distance (D) between two dams on both the time for impounding the downstream reservoir (T_{im}) and the time for breach development of the second dam (T_b). As shown in Figures 12a and 12b, T_{im} increased gradually with increasing H_d/H and D. This trend is primarily attributed to the enlargement of the downstream reservoir volume, which requires more time to fill. In terms of breach development time (T_b), the trend was more complex. When the distance between the dams was relatively short (D = 2.5 and 5.0 m), T_b first decreased and then increased with increasing relative height (H_d/H) (Figure 12c). However, when the dam spacing was larger (D = 7.5, 10.0, and 12.5 m), T_b consistently increased with increasing H_d/H. On the other hand, when examining the influence of dam spacing at fixed H_d/H values, no consistent relationship between T_b and D was observed (Figure 12d). These results suggest that both the discharge from the upstream dam at the moment of downstream dam failure and the size (or volume) of the downstream dam jointly influence T_b. Specifically, when the reservoir volume is relatively small, the downstream dam tends to fail

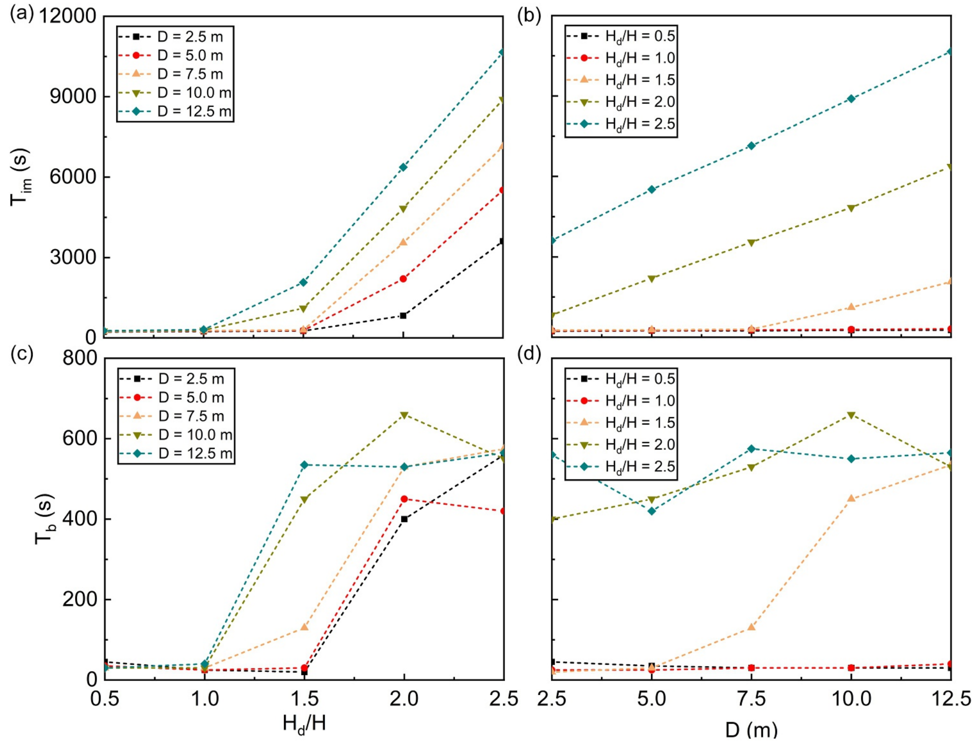

Figure 12. Variation of time for impounding the lake and time for peak discharge of the downstream dam under varying distances and relatively heights between two dams: (a) influence of relatively height on T_{im}; (b) influence of distance on T_{im}; (c) influence of relatively height on T_b and (d) influence of distance on T_b.

during the rising limb of the first dam's discharge curve. In this case, the increased inflow from the upstream dam accelerates the breach development, resulting in shorter T_b. However, when both H_d/H and D are sufficiently large, the reservoir volume of the downstream dam becomes the dominant factor controlling its failure, leading to longer T_b. Notably, a significant increase in T_b is consistently observed when H_d/H is around 1.5, as shown in Figures 12c and 12d. This behavior marks the transition from a cascading dam failure to a single dam failure, consistent with the mechanism previously discussed in Figure 11.

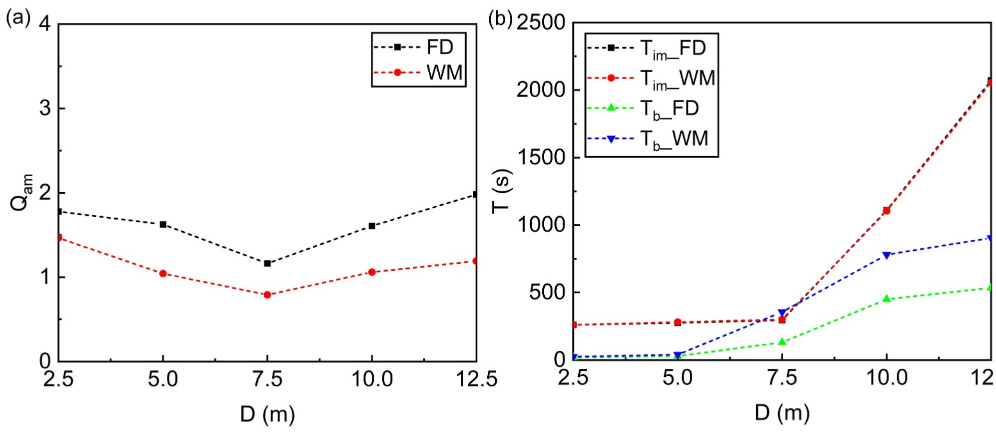

Figure 13. Variations of the discharge amplification index (Q_{am}), the time for impounding the lake (T_{im}) and the time for breach development (T_b) under varying material compositions: (a) the discharge amplification index; (b) the times for impounding the lake and breach development.

3.5. Influence of Material Composition of Downstream Dam

Figure 13 shows the variations of the discharge amplification index (Q_{am}), the time for impounding the lake (T_{im}) and the time for breach development (T_b) under fine-dominated and well-mixed material compositions. Similar to the scenarios considering fine-dominated material in the downstream dam, the discharge amplification index (Q_{am}) for the scenarios, where the relatively dam height (H_d/H) is 1.5 and the well-mixed material was considered in the downstream dam, varied from 0.79 to 1.47. Additionally, it first decreased and then increased with increasing the distance between two dams. However, compared to the fine-dominated dam, Q_{am} is much smaller for the dams consisting of well-mixed material under the same relatively height and distance between two dams (Figure 13a). For example, when H_d/H is 1.5 and D is 10 m, Q_{am} decrease from 1.61 to 1.06 with changing the downstream dam material from fine-dominated material composition to well-mixed one. Additionally, the minimum value of Q_{am}, where the peak discharge of the downstream dam was smaller than that of the upstream dam, can be observed when a distance of 7.5 m was considered. This difference in the amplification effect under vary material compositions is attributed to the dam failure process, and can be further explain by the values of T_{im} and T_b during the failure of the downstream dam. As shown in Figure 13b, under the same relatively height and distance between two dams, T_{im} remained nearly unchanged, while T_b increased substantially when the downstream dam material shifts from fine-dominated to well-mixed. In this case, although the impounded water volume remains constant, the increased breach development time reduces the peak discharge during the downstream dam failure, thereby leading to a lower Q_{am}.

4. Discussion

4.1. Factors That Control the Amplification Effect

Cascading dam failure can be summarized as the sequential failure of two or more dams, where the downstream dam fails under the influence of the unsteady flow and rapid reservoir filling generated by the upstream dam's breach. In this context, the factors influencing the failure of a single dam also contribute to the amplification effect observed during cascading failures. According to previous studies (T. Y. K. Chen & Capart, 2020; Macchione & Graziano, 2024; Walsh et al., 2021), these factors can be broadly classified into three categories: hydraulic parameters, dam parameters, and river channel parameters. The hydraulic parameter, particularly the inflow rate, has indeed significant influence of the peak discharge on single dam failure. Moreover, a significant amplification effect in the peak discharge can be observed when a cascading dam failure is considered. However, the discharge amplification index remained constant or even decreased slightly due to the simultaneous increase in Q_{p_down} and Q_{p_up}, as shown in Figure 9. This suggests that under varying inflow conditions, the amplification effect is predominantly governed by the failure characteristics of the upstream dam alone. Regarding dam parameters, they can be further divided into material composition and geometry. The former mainly affects dam's erodibility. The increase in the median diameter of dam material enhances the erosion susceptibility of the downstream dam, resulting in shorter breach durations and larger peak discharges, thus amplifying the cascading effect. In contrast, geometric parameters (e.g. H_d/H and D) influence the reservoir volume between the two dams. These factors determine the timing of the downstream dam's failure and the degree of interaction between the dams, both of which have significant implications for the amplification effect. Finally, river channel parameters, such as the bed slope and channel width, affect the flow dynamics and reservoir storage. Similar to dam geometry, these parameters influence the timing and nature of dam interactions by altering the intermediate reservoir volume. Consequently, the amplification effect arising from changes in dam geometry and river channel parameters can be interpreted as a result of different amplification mechanisms driven by varying reservoir characteristics.

Figure 14 illustrates the discharge hydrograph and the variation of the upstream water level during the failure of the upstream dam. The relationship between the reservoir volume and the discharge amplification index (Q_{am}) for all numerical scenarios involving fine-dominated materials is also depicted. It should be noted that the lake volume of the downstream dam is influenced not only by the height of the downstream dam and the distance between the two dams, but also by the height of the upstream dam at the moment the overflow onto the downstream dam begins, denoted here as H_{ub}. To characterize this interaction, we define the dimensionless parameter H_{ub}/H_d, where H_d is the downstream dam height. Two conditions arise from this ratio:

1. when $H_{\mathrm{ub}}/H_d > 1$, the water surface of the upstream dam is above the crest of the downstream dam, and thus the lake volume is equivalent to the entire reservoir volume between the two dams;

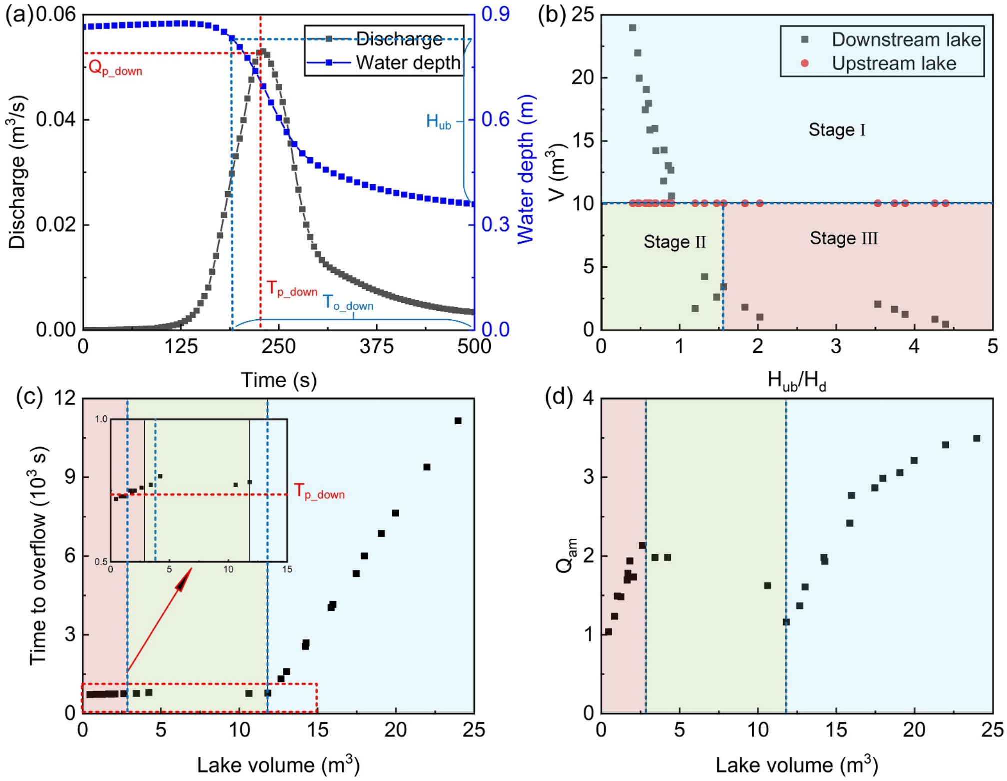

Figure 14. Relationship between the discharge amplification index (Q_{am}) and the volume of the downstream dam's reservoir: (a) Variation of discharge and upstream water level during the failure of the upstream dam; (b) relationship between lake volume of the downstream dam and H_{ub}/H_d; (c) relationship between the lake volume and the time to overflow of the downstream dam; (d) relationship between the lake volume of the downstream dam and the discharge amplification index (Q_{am}).

2. when $H_{\mathrm{ub}}/H_d < 1$, the downstream dam is not overtopped by the upstream flow at the beginning of failure, and therefore, part of the upstream reservoir volume contributes to the lake volume affecting the downstream dam.

Accordingly, the lake volume associated with the second dam can be calculated based on the value of H_{ub}/H_d, distinguishing whether the intermediate reservoir alone or a combined upstream volume influences the downstream failure process:

$$V_d = \begin{cases} \left(2D + \dfrac{2H_d}{\tan\vartheta}\right) \times \dfrac{1}{2}H_d \times 0.8, & \text{if } \dfrac{H_{\mathrm{ub}}}{H_d} > 1 \\ \left(2 \times (D + 12.93 + 3.62) + \dfrac{2H_d}{\tan\vartheta}\right) \times \dfrac{1}{2}H_d \times 0.8, & \text{if } \dfrac{H_{\mathrm{ub}}}{H_d} < 1 \end{cases} \quad (8)$$

where ϑ is the gradient of the second dam, D is the distance between two dams.

The relationship between the dimensionless parameter H_{ub}/H_d and the lake volume of the second dam is shown in Figure 14b. A significant change in the downstream lake volume is observed near $H_{\mathrm{ub}}/H_d = 1$, marking a transition in the control of the reservoir volume. Additionally, the volume of downstream lake is larger than that of the upstream lake when H_{ub}/H_d is smaller than 1. The relationships between lake volume, time to overflow and the discharge amplification index are shown in Figures 14c and 14d. Based on lake volume, similar variations can be observed in time to overflow of downstream dam and the discharge amplification index. Furthermore, three modes can be categorized: Mode I (red area, $H_{\mathrm{ub}}/H_d < 1$) corresponds to small lake volumes. Both the time to overflow of downstream dam and the Q_{am} increase with increasing lake volume. In this regime, the failure of the downstream dam typically occurs on the rising limb of the discharge curve from the upstream dam (see Figure 11a), and has no feedback effect on the upstream dam failure. In mode II (green area), where H_{ub}/H_d is

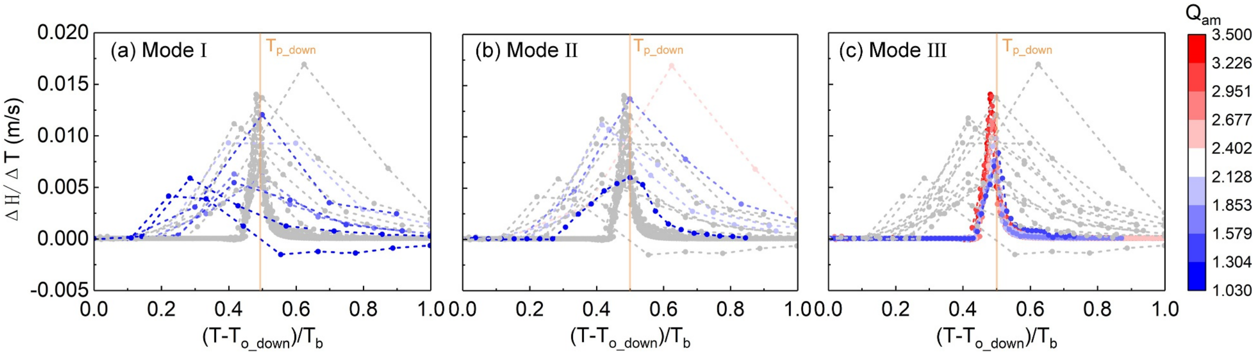

Figure 15. Erosion characteristics during the failure of the second dam in response to the three amplification modes (erosion point is located at the center of the upstream crest): (a) mode I; (b) mode II and (c) mode III. Note: erosion rate is calculated from the overtopping of the second dam (T_{o_down}) and with a duration of 2 (T_{p_down}–T_{o_down}). Each dot line in the figure represents the variation of erosion rate in each scenario, with gray dot lines corresponding to the scenarios which belong to the other amplification modes.

around 1 to 1.5, the system enters a transition phase where both the time to overflow of downstream dam and Q_{am} decrease with increasing lake volume. This is because the failure of the downstream dam tends to occur on the falling limb of the upstream dam's discharge curve (see Figure 11c), and its onset influences and controls the upstream dam failure. In this mode, a noticeable sudden drop appears in the upstream dam's discharge curve, and the overflow onto the downstream dam initiates at a lower discharge due to the larger lake volume. In mode III (blue area, $H_{ub}/H_d > 1.5$), the lake volume of the downstream dam is much larger than that of the upstream dam (Figure 14b). Under this circumstance, the failure process of the second dam becomes analogous to a single dam failure, where both the impounding time and the discharge increase with lake volume.

Furthermore, erosion characteristics during the failure of the downstream dam in response to the three amplification modes are analyzed (Figure 15). Under varying initial conditions and amplification modes, the erosion rate (defined as $\Delta H/\Delta T$) during the failure of the downstream dam first increases and then decreases until the end of dam failure. The peak erosion rate can be observed when the peak discharge is observed. Additionally, similarly to the variation of discharge amplification index (Q_{am}) in each amplification mode, the peak erosion rate varies accordingly. In particular, in mode I (Figure 15a), the peak erosion rate increases with increasing Q_{am}, while it decreases gradually in mode II (Figure 15b). In mode III, similar to the single dam failure, the peak erosion rate increases gradually with increasing the discharge during dam failure (Figure 15c).

4.2. Dam Failure Characteristics Under Unsteady Flow Condition

Another factor that contributes to the amplification effect is the unsteady flow generated by the upstream dam failure. To further investigate this effect, two numerical scenarios were designed based on the second Baige landslide dam, simulating dam failure under both steady and unsteady flow conditions. The dam geometry, model setup, input parameters, and numerical results under steady flow conditions were referenced from J. Yang et al. (2025). The inflow hydrographs used in both scenarios are shown in Figure 16a. For the unsteady flow condition, the inflow rate was designed to gradually increase to five times the constant value used in the steady flow scenario, before decreasing back to the original rate. The unsteady flow lasted for 61 hr, with the maximum inflow rate reached 27 hr after the initial increase from 800 m^3/s. The corresponding discharge variations during dam failure for both scenarios are presented in Figure 16b. Under steady flow conditions, the peak discharge of 32,767 m^3/s occurred at 187,200 s after the start of the simulation. In contrast, under unsteady flow conditions, the peak discharge increased to 35,246 m^3/s, occurring at 151,200 s. The dam failure under unsteady flow was triggered during the rising limb of the inflow hydrograph. Although the breach geometry at the time of peak discharge (e.g., breach width) was relatively similar between the two scenarios, a noticeably larger water depth was observed both upstream of the dam and within the diversion channel under the unsteady flow condition (Figures 16c and 16d).

Furthermore, two cross-sectional profiles and one point (A–A, B–B, and P, as shown in Figure 17b) along the flow direction in the diversion channel and across the dam crest were selected to further compare the dam failure processes under steady and unsteady flow conditions (Figure 17). The results indicate that dam failure progresses

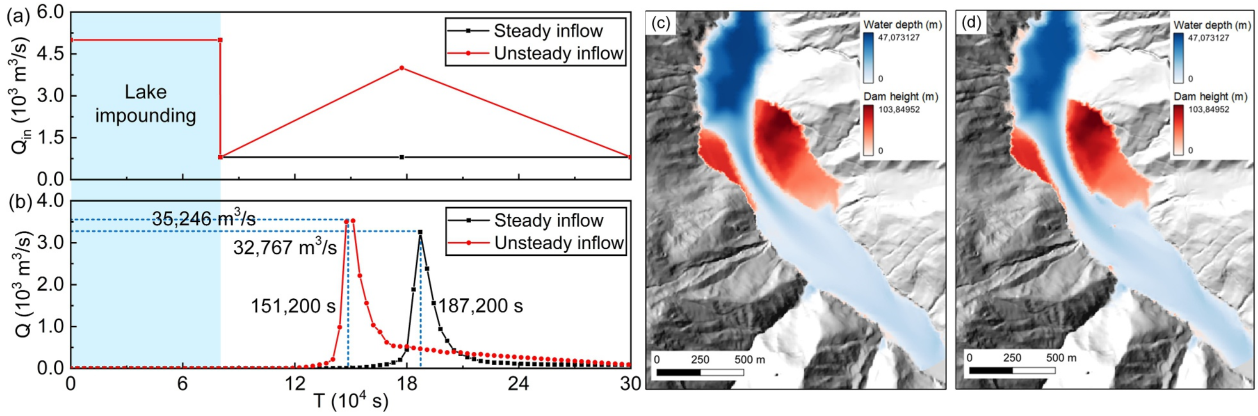

Figure 16. The failure of the second Baige landslide dam under steady and unsteady flow conditions: (a) the inflow curve; (b) variations of discharge during dam failure under varying conditions; (c) dam height and water level when peak discharge was observed under steady flow and (d) under unsteady flow.

more rapidly under unsteady flow. Specifically, under steady flow conditions, overtopping began 97,200 s after the start of the simulation, and the breach stabilized 100,000 s after overtopping. In contrast, under unsteady flow conditions, overtopping occurred earlier, at 93,600 s, and the breach stabilized significantly faster, within 60,000 s after overtopping. Additionally, a larger breach size and greater eroded volume were observed under unsteady flow conditions. These differences are attributed to the increased erosion rate resulting from the rising inflow during dam failure. As shown in Figures 17c and 17f, although similar trends can be observed in the variation of the erosion rate during dam failure, a larger peak erosion rate is observed when consider dam failure under unsteady flow condition. Consequently, a shorter duration is required to release the same volume of reservoir water, resulting in a higher peak discharge and a larger final breach size during dam failure. These factors further contribute to the amplification effect observed in cascading dam failure scenarios.

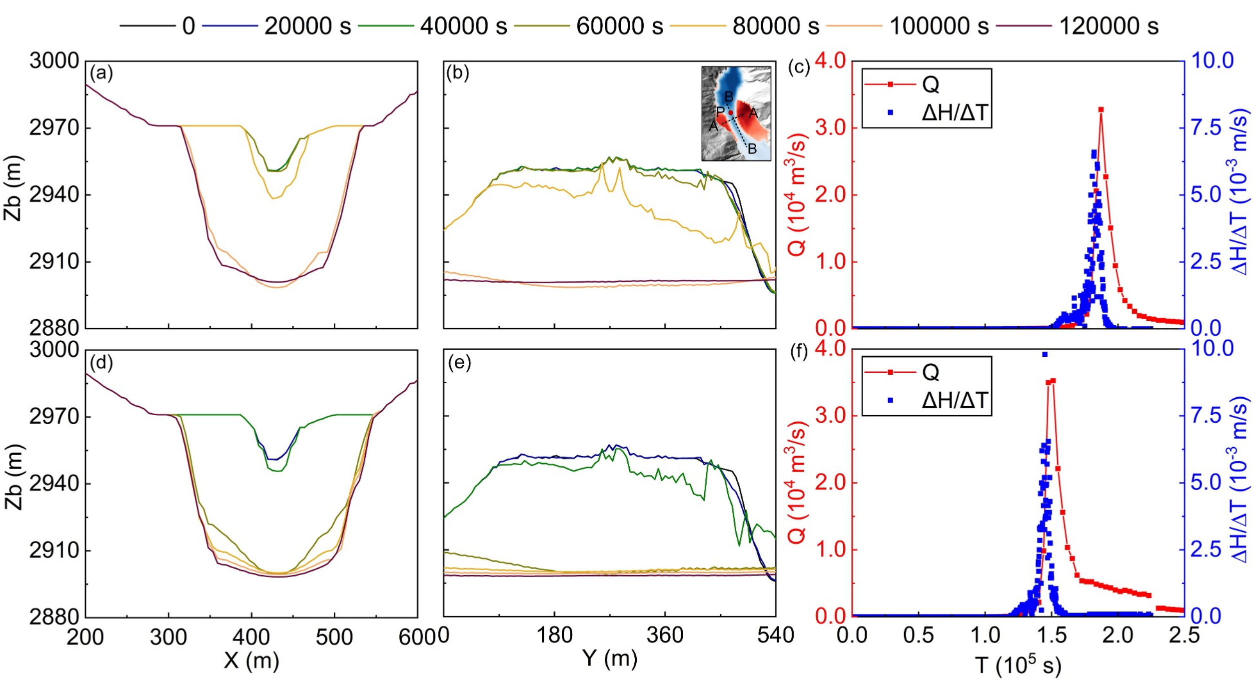

Figure 17. Dam failure process under steady and unsteady flow conditions: (a) profiles along A-A under steady flow; (b) profiles along B-B under steady flow; (c) erosion rate at point P during dam failure under steady flow; (d) profiles along A-A under unsteady flow; (e) profiles along B-B under unsteady flow and (f) erosion rate at point P during dam failure under unsteady flow. Note: $T = 0$ in (a, b, d and e) refers to the simulation time at 93,600 s, where overflow occurs under unsteady flow condition.

4.3. Limitations and Implications

Despite the insights provided by the numerical and experimental results, three limitations should be noted. The first limitation concerns the simplified bank failure module adopted in the numerical model (Figure 1c). The dam failure process can generally be characterized by two key mechanisms: surface erosion and breach widening (Alvarez et al., 2025; S. C. Chen et al., 2026; Coleman et al., 2002). Accurate simulation of these processes is essential for reliably predicting the rapid peak outflow during dam failure (Peng & Zhang, 2012; Schmitz et al., 2021; Swartenbroekx et al., 2010). The simplified bank failure module used in this study improves the representation of the dam failure process and thus contributes to a more accurate prediction of peak discharge (Figure 6). However, breach widening is inherently a stochastic slope failure process controlled by multiple factors, including soil type, water content, and degree of saturation (Walder et al., 2015; Walsh et al., 2021). Further development of the breach widening formulation, accounting for subsurface flows in the dike as suggested by Delpierre et al. (2023), are therefore required to better capture the dam failure dynamics and the resulting rapid outflow. A second limitation of the numerical model relates to material composition. In both the numerical simulations and laboratory experiments, only non-cohesive materials are considered. This simplification allows for good agreement between numerical and experimental results. Nevertheless, the presence of cohesive materials can significantly influence both surface erosion and breach widening by altering the evolution of material parameters during dam failure (Rifai et al., 2021; Zhao et al., 2014). Moreover, cohesive materials are widely observed in natural landslide dams and earthen embankments, highlighting the need to incorporate cohesion in future developments of the numerical model. The final limitation concerns scale effects associated with the sediments used in experimental setup. While Froude similarities is accurately applicable in pure hydrodynamic flows, achieving full similarity in dam failure experiments is inherently challenging due to differences in dam geometry, river channel characteristics, reservoir configuration, and material composition. Consequently, no direct prototype dam corresponds to the present experimental design. Nevertheless, several dimensionless parameters commonly used in physical modeling were applied to ensure that the experimental results are comparable to observations from real-world scenarios (see Text S2 in Supporting Information S1). Importantly, the results emphasize the critical influence of reservoir volume and downstream dam failure timing on the amplification effect. In practical applications, The findings of this study have important implications for hazard management in mountainous regions and for the assessment and mitigation of risks associated with dam systems along major river networks worldwide. Future efforts will integrate more advanced techniques, including remote sensing and numerical modeling, and are expected to enhance the monitoring, prediction, and understanding of cascading dam-failure processes in natural environments.

5. Conclusions

This study combined numerical and experimental modeling of cascading landslide dam failures to investigate the amplification effect of outburst floods. The influence of several key factors on the amplification effect was systematically quantified using three parameters: the discharge amplification index (Q_{am}), the times for impounding the lake (T_{im}) and for breach development (T_b) of the downstream dam. The results show that, under varying upstream inflow rates, the amplification effect is primarily governed by the failure characteristics of the upstream dam. Higher upstream inflow shorten T_{im} and T_b during downstream dam failure, ultimately leads to a larger peak discharge, and a slight decrease in Q_{am}. In contrast, under varying relative height and distance between the two dams, the amplification effect is strongly influenced by the interaction between two dams. This interaction is controlled by the downstream reservoir volume and the time when the downstream dam starts to fail, leading to more complex variations of Q_{am}, T_{im} and T_b. Three amplification modes were identified considering the dimensionless parameter H_{ub}/H_d, defined as the ratio between the heights of the upstream and downstream dams at the initiation of downstream dam overtopping. *Mode I* ($H_{\mathrm{ub}}/H_d < 1$) is characterized by a small downstream reservoir volume. In this mode, the downstream dam fails during the rising limb of the upstream dam's outflow hydrograph, and Q_{am} increases with increasing downstream lake volume. *Mode II* ($H_{\mathrm{ub}}/H_d = 1$–1.5) occurs when the downstream dam has a relatively large reservoir volume, but its height is comparable to the residual height of the upstream dam at the moment overflow begins. In this mode, the failure of the downstream dam significantly affects the upstream dam's failure, and Q_{am} decreases with an increasing downstream lake volume. *Mode III* ($H_{\mathrm{ub}}/H_d > 1.5$) corresponds to the scenarios in which the downstream lake volume is large enough for the downstream dam failure to become independent from the upstream dam failure and thus analogous to a single dam failure, and Q_{am} increases with increasing downstream lake volume. The amplification effect can also be interpreted from the

10.1029/2025WR042150

perspective of dam failure under unsteady inflow conditions. Experimental and field observations of dam failures under both steady and unsteady inflow conditions indicate that unsteady inflow generally produces higher erosion rates and shorter breach development durations. These effects result in larger peak discharges and therefore contribute to the amplification effect observed during cascading dam failures. Although limitations remain regarding the numerical model and the scale effects, the results still present valuable insights into the amplification effect during cascading dam failure. In particular, the findings highlight the critical role of reservoir volume and the unsteady flow generated by the failure of the upstream dam in controlling the amplification effect. These findings contribute to improved hazard management in mountainous regions and provide insights into risk assessment and mitigation strategies for dam systems along large rivers worldwide.

Notation

q	Flow discharge in the numerical model (m^3/s)
q_b, q_{bi}	Bedload transport rate for the total sediment and for each sediment fraction (m^3/s)
φ_a, φ_b	Interactions of bedload with bed and bank material, respectively (–)
φ_{ai}, φ_{bi}	Interaction of bedload with each fraction of the sediment bed and bank material (–)
φ_{si}	Interaction between the active layer and substrate layer in each fraction of the sediment (–)
α_{ca}, α_{cb}	Critical angles above and below the water level in the bank failure module (°)
α_{ra}, α_{rb}	Residual angles above and below the water level in the bank failure module (°)
Z_w, Z_b	Water level and bed level in the numerical model (m)
d_{50}, $d_{50,i}$	Median diameter of the total sediment and of each sediment fraction (mm)
P_{S}, P_{G}	Percentage content of sand and gravel fractions in the sediment (%)
ρ_d	Dry bulk density of the sediment (g/cm^3)
φ	Repose angle of the sediment (°)
C_u, C_c	Uniformity coefficient and curvature coefficient of the sediment (–)
e	Void ratio
Q_{in}	Upstream inflow rate (L/s)
n	Manning coefficient (sm$^{-1/3}$)
L, F	Number of sediment layer and sediment friction (–)
s	Relative specific gravity (–)
f	Porosity (–)
Q_{in}/Q	Non-dimensional inflow rate, with $Q = 1.13$ L/s (–)
H_d/H	Non-dimensional downstream dam height, with $H = 0.3$ m (–)
D	Distance between two dams (m)
V_u	Reservoir volume of the upstream dam (m^3)
V_d	Reservoir volume of the downstream dam (m^3)
Q_{et}, Q_{nt}	Discharge at time t in response to experimental and numerical results (m^3/s)
B_D, B_W	Breach depth and breach width (m)
Q_{am}	Discharge amplification index (–)
T_{im}	The impounding time of the downstream dam (s)

T_b	Time for breach development of the downstream dam (s)
Q_{p_down}, Q_{p_up}	Peak discharge during the failure of downstream and upstream dams (m^3/s)
T_{o_down}, T_{o_up}	Time when the downstream and upstream dams start to fail (s)
T_{p_down}, T_{p_up}	Time to peak discharge in response to the failure of downstream and upstream dams (s)
H_{ub}	The residual height of the first dam when the second dam starts to overflow (m)
θ	The gradient of the second dam (°)

Conflict of Interest

The authors declare no conflicts of interest relevant to this study.

Availability Statement

Data and relevant Python script for data processing are publicly available at Zenodo via (J. Yang, 2026, https://doi.org/10.5281/zenodo.18268019).

Acknowledgments
We acknowledge funding from the National Science Foundation of China (No. 42307196) and the National Key R&D Program of China (No. 2023YFC3008300).

References

Abad, L., Hölbling, D., Spiekermann, R., Prasicek, G., Dabiri, Z., & Argentin, A. L. (2022). Detecting landslide-dammed lakes on Sentinel-2 imagery and monitoring their spatio-temporal evolution following the Kaikōura earthquake in New Zealand. *Science of the Total Environment*, *820*, 153335. https://doi.org/10.1016/j.scitotenv.2022.153335

Al Mehedi, M. A., Saki, S., Patel, K., Shen, C., Cohen, S., Smith, V., et al. (2024). Spatiotemporal variability of channel roughness and its substantial impacts on flood modeling errors. *Earth's Future*, *12*(7), e2023EF004257. https://doi.org/10.1029/2023EF004257

Alvarez, T., Ferreira, R. M., Mendes, S., Aleixo, R., Amaral, S., Caldeira, L., & Viseu, T. (2025). Breaching of homogeneous dams with internal drainage system. *Water Resources Research*, *61*(7), e2024WR038552. https://doi.org/10.1029/2024WR038552

Cao, Z., Yue, Z., & Pender, G. (2011). Flood hydraulics due to cascade landslide dam failure. *Journal of Flood Risk Management*, *4*(2), 104–114. https://doi.org/10.1111/j.1753-318X.2011.01098.x

Carrivick, J. L., & Tweed, F. S. (2016). A global assessment of the societal impacts of glacier outburst floods. *Global and Planetary Change*, *144*, 1–16. https://doi.org/10.1016/j.gloplacha.2016.07.001

Casagli, N., Ermini, L., & Rosati, G. (2003). Determining grain size distribution of the material composing landslide dams in the Northern Apennines: Sampling and processing methods. *Engineering Geology*, *69*(1–2), 83–97. https://doi.org/10.1016/S0013-7952(02)00249-1

Chang, D. S., & Zhang, L. M. (2010). Simulation of the erosion process of landslide dams due to overtopping considering variations in soil erodibility along depth. *Natural Hazards and Earth System Sciences*, *10*(4), 933–946. https://doi.org/10.5194/nhess-10-933-2010

Chen, S., Chen, Z., Tao, R., Yu, S., Xu, W., Zhou, X., & Zhou, Z. (2018). Emergency response and back analysis of the failures of earthquake triggered cascade landslide dams on the Mianyuan River, China. *Natural Hazards Review*, *19*(3), 05018005. https://doi.org/10.1061/(ASCE)NH.1527-6996.0000285

Chen, S. C., Hung, C. Y., Chen, P. Y., Tfwala, S. S., Liang, M. C., Jiang, C. H., & Chao, W. A. (2026). Synchronized multidisciplinary observations in large-scale dam breach experiments to enhance the understanding of dam failure evolution. *Water Resources Research*, *62*(1), e2025WR040786. https://doi.org/10.1029/2025WR040786

Chen, T. Y. K., & Capart, H. (2020). Kinematic wave solutions for dam-break floods in non-uniform valleys. *Journal of Hydrology*, *582*, 124381. https://doi.org/10.1016/j.jhydrol.2019.124381

Coleman, S. E., Andrews, D. P., & Webby, M. G. (2002). Overtopping breaching of noncohesive homogeneous embankments. *Journal of Hydraulic Engineering*, *128*(9), 829–838. https://doi.org/10.1061/(ASCE)0733-9429(2002)128:9(829)

Costa, J. E., & Schuster, R. L. (1988). The formation and failure of natural dams. *Geological Society of America Bulletin*, *100*(7), 1054–1068. https://doi.org/10.1130/0016-7606(1988)100<1054:TFAFON>2.3.CO;2

Cui, P., Zhou, G. G., Zhu, X. H., & Zhang, J. Q. (2013). Scale amplification of natural debris flows caused by cascading landslide dam failures. *Geomorphology*, *182*, 173–189. https://doi.org/10.1016/j.geomorph.2012.11.009

Dai, S., Yang, S., Zhang, Y., He, X., Li, Z., Liu, Y., et al. (2025). Numerical study of impact pressure and force of cascading dam-break floods on the downstream dam. *Journal of Hydrology*, *648*, 132360. https://doi.org/10.1016/j.jhydrol.2024.132360

Dazzi, S., Vacondio, R., & Mignosa, P. (2019). Integration of a levee breach erosion model in a GPU-accelerated 2D shallow water equations code. *Water Resources Research*, *55*(1), 682–702. https://doi.org/10.1029/2018WR023826

Delpierre, N., Rattez, H., & Soares-Frazao, S. (2023). Finite-volume coupled surface-subsurface flow modelling in Earth dikes. *Journal of Hydraulic Research*, *61*(5), 754–763. https://doi.org/10.1080/00221686.2023.2246936

Ermini, L., & Casagli, N. (2003). Prediction of the behaviour of landslide dams using a geomorphological dimensionless index. *Earth Surface Processes and Landforms*, *28*(1), 31–47. https://doi.org/10.1002/esp.424

Fan, X., Tang, C. X., Van Westen, C. J., & Alkema, D. (2012). Simulating dam-breach flood scenarios of the Tangjiashan landslide dam induced by the Wenchuan Earthquake. *Natural Hazards and Earth System Sciences*, *12*(10), 3031–3044. https://doi.org/10.5194/nhess-12-3031-2012

Ferrari, A., Vacondio, R., & Mignosa, P. (2023). High-resolution 2D shallow water modelling of dam failure floods for emergency action plans. *Journal of Hydrology*, *618*, 129192. https://doi.org/10.1016/j.jhydrol.2023.129192

Geertsema, M., Menounos, B., Bullard, G., Carrivick, J. L., Clague, J. J., Dai, C., et al. (2022). The 28 November 2020 landslide, tsunami, and outburst flood–A hazard cascade associated with rapid deglaciation at Elliot Creek, British Columbia, Canada. *Geophysical Research Letters*, *49*(6), e2021GL096716. https://doi.org/10.1029/2021GL096716

Gregoretti, C., Maltauro, A., & Lanzoni, S. (2010). Laboratory experiments on the failure of coarse homogeneous sediment natural dams on a sloping bed. *Journal of Hydraulic Engineering*, *136*(11), 868–879. https://doi.org/10.1061/(ASCE)HY.1943-7900.0000259

Guan, S., Shi, Z., Zheng, H., Shen, D., Hanley, K. J., Yang, J., & Xia, C. (2023). Effects of soil properties and geomorphic parameters on the breach mechanisms of landslide dams and prediction of peak discharge. *Acta Geotechnica*, *18*(10), 5485–5502. https://doi.org/10.1007/s11440-023-01908-2

Haces-Garcia, F., Kotzamanis, V., Glennie, C. L., & Rifai, H. S. (2025). Improving Manning's n in flood models using 3D point clouds, flume experiments, and deep learning. *Water Resources Research*, *61*(3), e2024WR037665. https://doi.org/10.1029/2024WR037665

Hu, W., Li, Y., Fan, Y., Xiong, M., Luo, H., McSaveney, M., et al. (2022). Flow amplification from cascading landslide dam failures: Insights from flume experiments. *Engineering Geology*, *297*, 106483. https://doi.org/10.1016/j.enggeo.2021.106483

Korup, O. (2004). Geomorphometric characteristics of New Zealand landslide dams. *Engineering Geology*, *73*(1–2), 13–35. https://doi.org/10.1016/j.enggeo.2003.11.003

Liu, N., Chen, Z., Zhang, J., Lin, W., Chen, W., & Xu, W. (2010). Draining the Tangjiashan barrier lake. *Journal of Hydraulic Engineering*, *136*(11), 914–923. https://doi.org/10.1061/(ASCE)HY.1943-7900.0000241

Macchione, F., & Graziano, A. A. (2024). Dimensionless attenuation of dam-breach flood wave propagating along a river. *Journal of Hydrology*, *641*, 131765. https://doi.org/10.1016/j.jhydrol.2024.131765

Martínez-Aranda, S., Murillo, J., & García-Navarro, P. (2022). A GPU-accelerated Efficient Simulation Tool (EST) for 2D variable-density mud/debris flows over non-uniform erodible beds. *Engineering Geology*, *296*, 106462. https://doi.org/10.1016/j.enggeo.2021.106462

Mergili, M., Emmer, A., Juřicová, A., Cochachin, A., Fischer, J. T., Huggel, C., & Pudasaini, S. P. (2018). How well can we simulate complex hydro-geomorphic process chains? The 2012 multi-lake outburst flood in the Santa Cruz Valley (Cordillera Blanca, Perú). *Earth Surface Processes and Landforms*, *43*(7), 1373–1389. https://doi.org/10.1002/esp.4318

Meurice, R., & Soares-Frazão, S. (2020). A 2D HLL-based weakly coupled model for transient flows on mobile beds. *Journal of Hydroinformatics*, *22*(5), 1351–1369. https://doi.org/10.2166/hydro.2020.033

Morris, M., Hanson, G., & Hassan, M. (2008). Improving the accuracy of breach modelling: Why are we not progressing faster? *Journal of Flood Risk Management*, *1*(3), 150–161. https://doi.org/10.1111/j.1753-318X.2008.00017.x

Nardini, O., Confuorto, P., Intrieri, E., Montalti, R., Montanaro, T., Robles, J. G., et al. (2024). Integration of satellite SAR and optical acquisitions for the characterization of the Lake Sarez landslides in Tajikistan. *Landslides*, *21*(6), 1385–1401. https://doi.org/10.1007/s10346-024-02214-y

Peng, M., & Zhang, L. M. (2012). Breaching parameters of landslide dams. *Landslides*, *9*(1), 13–31. https://doi.org/10.1007/s10346-011-0271-y

Rifai, I., El Kadi Abderrezzak, K., Hager, W. H., Erpicum, S., Archambeau, P., Violeau, D., et al. (2021). Apparent cohesion effects on overtopping-induced fluvial dike breaching. *Journal of Hydraulic Research*, *59*(1), 75–87. https://doi.org/10.1080/00221686.2020.1714760

Rifai, I., Erpicum, S., Archambeau, P., Violeau, D., Pirotton, M., El Kadi Abderrezzak, K., & Dewals, B. (2017). Overtopping induced failure of noncohesive, homogeneous fluvial dikes. *Water Resources Research*, *53*(4), 3373–3386. https://doi.org/10.1002/2016WR020053

Sattar, A., Cook, K. L., Rai, S. K., Berthier, E., Allen, S., Rinzin, S., et al. (2025). The Sikkim flood of October 2023: Drivers, causes, and impacts of a multihazard cascade. *Science*, *387*(6740), eads2659. https://doi.org/10.1126/science.ads2659

Schmitz, V., Arnst, M., El kadi Abderrezzak, K., Pirotton, M., Erpicum, S., Archambeau, P., & Dewals, B. (2023). Global sensitivity analysis of a dam breaching model: To which extent is parameter sensitivity case-dependent? *Water Resources Research*, *59*(6), e2022WR033894. https://doi.org/10.1029/2022WR033894

Schmitz, V., Erpicum, S., El Kadi Abderrezzak, K., Rifai, I., Archambeau, P., Pirotton, M., & Dewals, B. (2021). Overtopping-induced failure of non–cohesive homogeneous fluvial dikes: Effect of dike geometry on breach discharge and widening. *Water Resources Research*, *57*(7), e2021WR029660. https://doi.org/10.1029/2021WR029660

Shen, D., Shi, Z., Yang, J., Zheng, H., & Zhu, F. (2024). Qualitative analysis of the overtopping-induced failure of noncohesive landslide dams: Effect of material composition and dam structure on breach mechanisms. *Journal of Hydrology*, *638*, 131580. https://doi.org/10.1016/j.jhydrol.2024.131580

Shi, Z. M., Guan, S. G., Peng, M., Zhang, L. M., Zhu, Y., & Cai, Q. P. (2015). Cascading breaching of the Tangjiashan landslide dam and two smaller downstream landslide dams. *Engineering Geology*, *193*, 445–458. https://doi.org/10.1016/j.enggeo.2015.05.021

Shugar, D. H., Burr, A., Haritashya, U. K., Kargel, J. S., Watson, C. S., Kennedy, M. C., et al. (2020). Rapid worldwide growth of glacial lakes since 1990. *Nature Climate Change*, *10*(10), 939–945. https://doi.org/10.1038/s41558-020-0855-4

Soares-Frazao, S., Canelas, R., Cao, Z., Cea, L., Chaudhry, H. M., Die Moran, A., et al. (2012). Dam-break flows over mobile beds: Experiments and benchmark tests for numerical models. *Journal of Hydraulic Research*, *50*(4), 364–375. https://doi.org/10.1080/00221686.2012.689682

Swartenbroekx, C., Soares-Frazão, S., Staquet, R., & Zech, Y. (2010). Two-dimensional operator for bank failures induced by water-level rise in dam-break flows. *Journal of Hydraulic Research*, *48*(3), 302–314. https://doi.org/10.1080/00221686.2010.481856

Takayama, S., Fujimoto, M., & Satofuka, Y. (2021). Amplification of flood discharge caused by the cascading failure of landslide dams. *International Journal of Sediment Research*, *36*(3), 430–438. https://doi.org/10.1016/j.ijsrc.2020.10.007

van den Bout, B., Tang, C., van Westen, C., & Jetten, V. (2022). Physically-based modelling of co-seismic landslide, debris flow and flood cascade. *Natural Hazards and Earth System Sciences Discussions*, *2022*, 1–56. https://doi.org/10.5194/nhess-22-3183-2022

Veh, G., Lützow, N., Kharlamova, V., Petrakov, D., Hugonnet, R., & Korup, O. (2022). Trends, breaks, and biases in the frequency of reported glacier lake outburst floods. *Earth's Future*, *10*(3), e2021EF002426. https://doi.org/10.1029/2021EF002426

Walder, J. S., Iverson, R. M., Godt, J. W., Logan, M., & Solovitz, S. A. (2015). Controls on the breach geometry and flood hydrograph during overtopping of noncohesive earthen dams. *Water Resources Research*, *51*(8), 6701–6724. https://doi.org/10.1002/2014WR016620

Walder, J. S., & O'Connor, J. E. (1997). Methods for predicting peak discharge of floods caused by failure of natural and constructed earthen dams. *Water Resources Research*, *33*(10), 2337–2348. https://doi.org/10.1029/97WR01616

Walsh, A., McDougall, S., Evans, S. G., & Take, W. A. (2021). Effect of upstream dam geometry on peak discharge during overtopping breach in noncohesive homogeneous embankment dams; implications for Tailings dams. *Water Resources Research*, *57*(12), e2020WR029358. https://doi.org/10.1029/2020WR029358

Wu, W. (2013). Simplified physically based model of earthen embankment breaching. *Journal of Hydraulic Engineering*, *139*(8), 837–851. https://doi.org/10.1061/(ASCE)HY.1943-7900.0000741

Yang, J. (2026). Amplification of outburst floods during cascading landslide dam failures: Insights from numerical and experimental modelling [Dataset]. *Zenodo*. https://doi.org/10.5281/zenodo.18268019

Yang, J., Shen, D., Shi, Z., & Soares-Frazão, S. (2025). Detailed numerical simulation of landslide dam failure considering non-uniform and multi-layered sediments: A case study of the second Baige landslide dam in the Jinsha River, China. *Earth Surface Processes and Landforms*, *50*(7), e70097. https://doi.org/10.1002/esp.70097

Yang, J., Shi, Z., Peng, M., Zheng, H., Soares-Frazão, S., Zhou, J., et al. (2022). Quantitative risk assessment of two successive landslide dams in 2018 in the Jinsha River, China. *Engineering Geology*, *304*, 106676. https://doi.org/10.1016/j.enggeo.2022.106676

Yang, J., Soares-Frazao, S., Shi, Z., & Shen, D. (2024). A 2D numerical model for simulating landslide dam failure and induced morphological changes considering multi-layer and non-uniform sediments. *Journal of Hydroinformatics*, *26*(7), 1606–1628. https://doi.org/10.2166/hydro.2024.103

Yang, Q., Guan, M., Peng, Y., & Chen, H. (2020). Numerical investigation of flash flood dynamics due to cascading failures of natural landslide dams. *Engineering Geology*, *276*, 105765. https://doi.org/10.1016/j.enggeo.2020.105765

Yanites, B. J., Clark, M. K., Roering, J. J., West, A. J., Zekkos, D., Baldwin, J. W., et al. (2025). Cascading land surface hazards as a nexus in the Earth system. *Science*, *388*(6754), eadp9559. https://doi.org/10.1126/science.adp9559

Zhao, G., Visser, P. J., Peeters, P., & Vrijling, J. K. (2014). Hydrodynamic erosion in cohesive embankment breach. In L. Cheng, S. Draper, & H. An (Eds.), *Scour and erosion* (pp. 441–445). CRC Press.

Zheng, H., Shi, Z., Peng, M., Guan, S., Hanley, K. J., & Feng, S. (2022). Amplification effect of cascading breach discharge of landslide dams. *Landslides*, *19*(3), 573–587. https://doi.org/10.1007/s10346-021-01816-0

Zhong, Q. M., Chen, S. S., Mei, S. A., & Cao, W. (2018). Numerical simulation of landslide dam breaching due to overtopping. *Landslides*, *15*(6), 1183–1192. https://doi.org/10.1007/s10346-017-0935-3

Zhou, G. G., Cui, P., Chen, H. Y., Zhu, X. H., Tang, J. B., & Sun, Q. C. (2013). Experimental study on cascading landslide dam failures by upstream flows. *Landslides*, *10*(5), 633–643. https://doi.org/10.1007/s10346-012-0352-6

Zhou, G. G., Cui, P., Zhu, X., Tang, J., Chen, H., & Sun, Q. (2015). A preliminary study of the failure mechanisms of cascading landslide dams. *International Journal of Sediment Research*, *30*(3), 223–234. https://doi.org/10.1016/j.ijsrc.2014.09.003

Zhou, G. G., Lu, X., Xie, Y., Cui, K. F., & Tang, H. (2022). Mechanisms of the non-uniform breach morphology evolution of landslide dams composed of unconsolidated sediments during overtopping failure. *Journal of Geophysical Research: Earth Surface*, *127*(10), e2022JF006664. https://doi.org/10.1029/2022JF006664